One-Pot Synthesis and Structural Evolution of Colloidal Cesium Lead Halide – Lead Sulfide Heterostructure Nanocrystals for Optoelectronic Applications

Metikoti Jagadeeswararao[§,¶], Parth Vashishtha[†], Thomas J.N. Hooper[‡], Anil Kanwat[§], Jia Wei Melvin Lim [‖, #], Sujaya Kumar Vishwanath[†], Natalia Yantara[§], Taewook Park[¶], Tze Chien Sum [‖], Dae Sung Chung[¶], Subodh G. Mhaisalkar[§], and Nripan Mathews[†, §]*

[§]*Energy Research Institute @ NTU (ERIAN), Nanyang Technological University, 50 Nanyang Drive, Singapore 637553, Singapore*

† School of Materials Science and Engineering, Nanyang Technological University (NTU), 50 Nanyang Avenue, Singapore 639798, Republic of Singapore

‡ Center of High Field NMR Spectroscopy and Imaging, Nanyang Technological University, 21 Nanyang Link, Singapore 637371

[‖]*Division of Physics and Applied Physics, School of Physical and Mathematical Sciences, Nanyang Technological University, Singapore 637371, Singapore*

[#] *Energy Research Institute @NTU (ERI@N), Interdisciplinary Graduate Programme, Nanyang Technological University, Singapore 637371, Singapore*

[¶]*Department of Chemical Engineering, Pohang University of Science and Technology (POSTECH), Pohang 37363, Republic of Korea*

Corresponding Author: E-mail: Nripan@ntu.edu.sg

Abstract

Heterostructures, combining perovskite nanocrystals (PNC) and chalcogenide quantum dots, could pave a path to optoelectronic device applications by enabling absorption in the near infra-red region, tailorable electronic properties, and stable crystal structures. Ideally, the heterostructure host material requires a similar lattice constant as the guest which is also constrained by the synthesis protocol and materials selectivity. Herein, we present an efficient one-pot hot-injection method to synthesize colloidal all-inorganic cesium lead halide – lead sulfide ($CsPbX_3$ (X=Cl, Br, I)-PbS) heterostructure nanocrystals (HNCs) via the epitaxial

growth of the perovskite onto the pre-synthesized PbS nanocrystals (NCs). Optical and structural characterization evidenced the formation of heterostructures. The embedding of PbS NCs into $CsPbX_3$ perovskite allows the tuning of the absorption and emission from 400 nm to 1100 nm by tuning the size and composition of perovskite HNCs. The $CsPbI_3$-PbS HNCs show enhanced stability in ambient conditions. The stability, tunable optical properties and the variable band alignments accessible in this system would have implications in the design of novel optoelectronic applications such as light-emitting diodes, photodetectors, photocatalysis and photovoltaics.

TOC Graphic

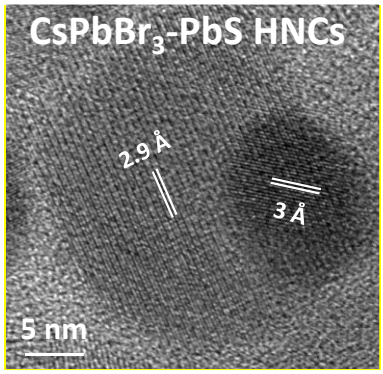

Metal halide perovskite nanocrystals (PNCs) exhibit exciting optoelectronic properties for numerous device applications, including solar cells, light-emitting diodes, photodetectors, and lasers owing to their narrow emission line-widths, high photoluminescence quantum yields (PLQYs), low defect densities, and high absorption coefficients.[1-15] PNCs benefit from the advantage of quantum confinement and size/composition tunable optical properties.[14, 16-20] Their optoelectronic properties can also be enhanced by incorporating transition or lanthanide metal ions in the perovskite matrix, extending emission in the visible and near-infrared (NIR) regions and boosting PLQY.[20-22] However, despite having high PLQY, the stability of organic-inorganic PNCs ($MPbX_3$ where M is $CH_3NH_3^+$ or $HC(NH_2)_2^+$ and X is Cl^-, Br^-, or I^-) are limited by poor thermal stability and volatility of the organic cations.[23] Alternatively, fully inorganic PNCs ($CsPbX_3$) have been used to enhance their thermal stability,[24-25] Still, surface defect

density and ion migration limit the environmental stability of inorganic lead halide PNCs. Thus, there is a need to stabilize the inorganic nanocrystals (NCs).[26-28] Some attempts have been made to protect NCs from moisture penetration and thermal stress by making heterostructures (i.e. core/shell or composite) with various materials, i.e., inorganic or organic matrix of silica, silica/alumina monolith, amorphous alumina, TiO_2, polymers, and metal-organic frameworks. [27, 29-33] In other attempts, NCs were alloyed with Mn^{2+}, Zn^{2+} metal ions to enhance the perovskite phase stability.[34-36]

A recent study demonstrated the introduction of PbS into the perovskite can be possible due to similar lattice constant and related crystal structures (For instance, the crystal structures of $MAPbI_3$ and PbS are tetragonal and rock-salt, respectively and Pb being a hexa-coordinated in each crystal.[37,42] Moreover, a shell of PbS onto the perovskite improves black phase stability of iodide-based perovskite and reduces ionic migration in the mixed perovskite system.[37-38] These particles show extended optical response and modulation of the electronic properties from n-type to ambipolar transport, with implications for photodetector, photovoltaic, and NIR LED applications. [39-41] Sargent et al, and other researchers reported another study by embedding the PbS NCs into the bulk matrix of perovskite (hybrid and all-inorganic) for improved optoelectronic properties and the phase stability of iodide based perovskite.[37, 42-44] The size and composition of the $CsPbX_3$ NCs and its relative alignment to the band structure of PbS could form two types of energy band alignment, named type-I and type-II. Type I promotes energy transfer to PbS, and type II promotes carrier separation across the interface. Recently, Zhang et al. have shown the possibility of forming a type-I $CsPbBr_3$-PbS heterostructure NCs (HNCs) via post-synthesis treatment for tunable emission in the visible and NIR regions.[45] However, the synthetic protocol requires a long processing time (~24hrs) along with the formation of a 0D (Cs_4PbBr_6) impurity phase. Thus, there is a need to develop

a simple synthesis protocol for $CsPbX_3$-PbS HNCs and examine its influence on optoelectronic properties as well as the stability of their crystal structures.

Herein, we report a one-pot hot-injection method for the synthesis of colloidal $CsPbX_3$-PbS HNCs by growing $CsPbX_3$ NCs onto the preformed PbS NCs in different halide environments. Extensive structural characterization such as high-resolution transmission electron microscopy (HR-TEM), X-ray diffraction (XRD), and solid-state NMR as well as optical characterization have been performed to analyze the formation of HNCs. Ultraviolet photoelectron spectroscopy (UPS) is utilized to examine the type-I and type-II heterojunction of $CsPbBr_3$-PbS and $CsPbI_3$-PbS HNCs. Lastly, the PbS embedded HNCs offer enhanced optical and structural stability along with high PLQY compared to that of perovskite $CsPbX_3$ NCs.

$CsPbBr_3$-PbS HNCs were prepared via a hot injection method following La Mer's model for synthesizing colloidal NCs (Fig. S1). The full synthesis methodology is detailed within the supporting information (SI), alongside images of the reaction color changes (Fig. S2). Thioacetamide was dispersed in oleylamine (OLA) at room temperature and this mixture was used as a sulfur precursor with a concentration of 5 wt% to $PbBr_2$. The sulfur precursor was added into the $PbBr_2$ solution in 1-octadecene (ODE) along with OLA and oleic acid (OA) at 135 ^oC as shown in Scheme 1(i). Immediately the colorless solution turns brown as shown in Scheme 1(ii). This color change indicates the formation of PbS NCs. After which, the reaction temperature was raised to 160 ^oC. The quick injection of Cs-oleate precursor into the above reaction mixture leads to the formation of a dark green color solution as shown in Scheme 1(iii), indicating the formation of $CsPbBr_3$-PbS HNCs. $CsPbI_3$-PbS and $CsPbCl_3$-PbS HNCs were also prepared by injecting the sulfur precursor into the respective lead iodide (PbI_2) and lead chloride ($PbCl_2$) source as described in the SI. For comparison, $CsPbX_3$ NCs were also synthesized by a similar hot injection method.

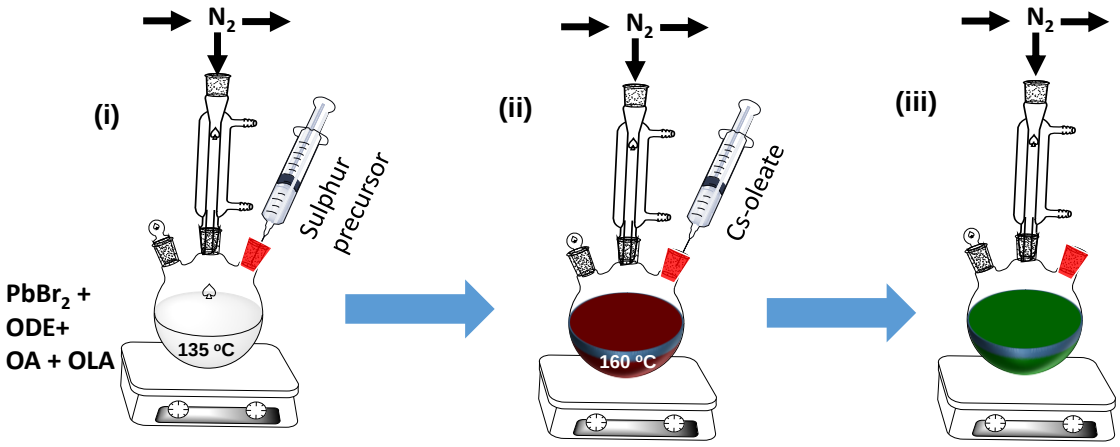

Scheme 1. Shows the synthesis of $CsPbBr_3$-PbS heterostructure NCs (HNCs) by a hot-injection method. (i) consists of $PbBr_2$ solution in 1-octadecene (ODE), oleic acid (OA), oleylamine (OLA). (ii) PbS NCs formation after injection of the sulfur precursor into $PbBr_2$ solution. (iii) $CsPbBr_3$-PbS HNCs formation after injection of Cs-oleate into PbS NCs solution.

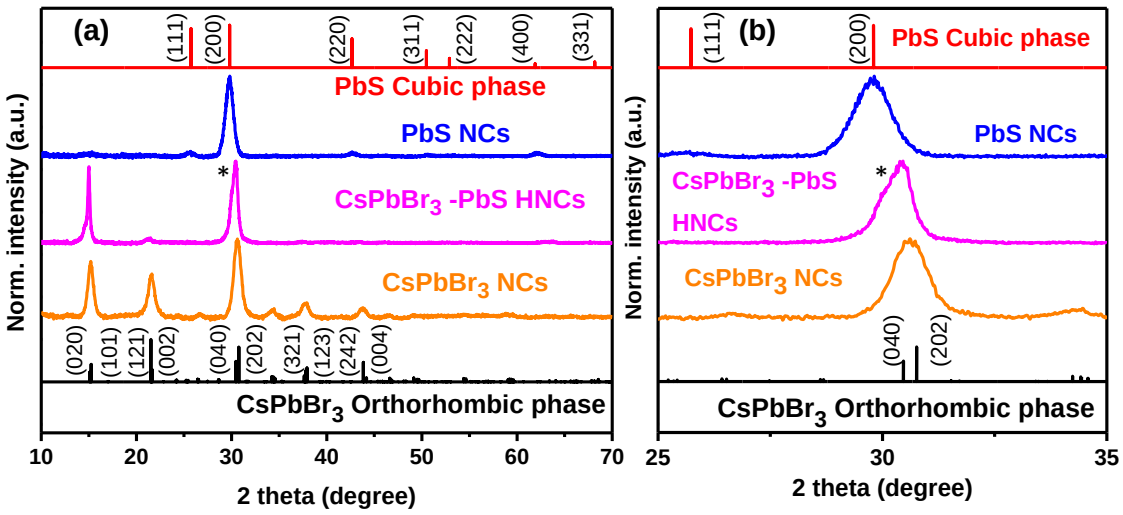

Fig. 1 a) Powder X-ray diffraction (XRD) patterns of $CsPbBr_3$, $CsPbBr_3$-PbS HNCs and PbS NCs. Bulk reference patterns of $CsPbBr_3$ with the orthorhombic phase with reference number (96-451-0746) and PbS with cubic phase with reference number (04-004-5639) have also been provided for the reference. For the orthorhombic phase of bulk $CsPbBr_3$, only major peaks were shown. b) shows the zoom-in spectra of Fig. 1a in the 2θ range 25-35° to see the changes in peak position at 29.8°.

To verify the formation of $CsPbBr_3$-PbS heterostructures, XRD patterns have been collected. Fig. 1a shows the XRD pattern of $CsPbBr_3$ NCs, PbS NCs, and $CsPbBr_3$-PbS HNCs along with

the reference patterns for bulk $CsPbBr_3$ and PbS. The diffraction patterns for $CsPbBr_3$ NCs indicate a wide distribution of orthorhombic planes as shown in Fig. 1a[30, 46] which reduces to mainly three planes upon PbS incorporation in $CsPbBr_3$-PbS HNCs. $CsPbBr_3$-PbS HNCs exhibit diffraction patterns similar to the $CsPbBr_3$, however, it is difficult to distinguish between the orthorhombic phase and cubic phase due to the broadening of XRD peaks of $CsPbBr_3$-PbS HNCs. Interestingly, the XRD peak of $CsPbBr_3$ at ~21.5° significantly reduces in intensity while ~15.2° and ~30.7° peaks gain intensity upon PbS incorporation. To further verify this synergetic effect, less amount of PbS (2%) was incorporated into $CsPbBr_3$, which results in a little more intense peak at ~21.5° than the 5% PbS sample as shown in Fig. S3. This suggesting that the addition of excess sulfur precursor allowing $CsPbBr_3$-PbS HNCs to grow in the direction of planes at ~15.2° and ~30.7°. A shoulder diffraction peak starts to emerge at 29.8°, as shown in Fig. 1b (highlighted by a *), which asserts the presence of cubic PbS phase. The co-existence of PbS (200) plane and $CsPbBr_3$ (202) plane confirm the formation of $CsPbBr_3$-PbS HNCs. The distinct XRD diffraction peak arises at 29.8° in $CsPbI_3$-PbS and $CsPbCl_3$-PbS HNCs than $CsPbI_3$ and $CsPbCl_3$, respectively, further verifies the successful incorporation of PbS in $CsPbX_3$-PbS HNCs (Fig. S4a, b, c).

To verify the morphology and size of NCs, transmission electron microscopy (TEM) measurements have been carried out. Fig. 2a shows the TEM image of $CsPbBr_3$ NCs depicting the characteristic cubic morphology of NCs. The HRTEM image with an interplanar distance of 4.0 Å shown in Fig. 2b corresponds to (002) plane at $2\theta=21.68°$ confirming the formation of orthorhombic phase in $CsPbBr_3$ perovskite NCs.[46]

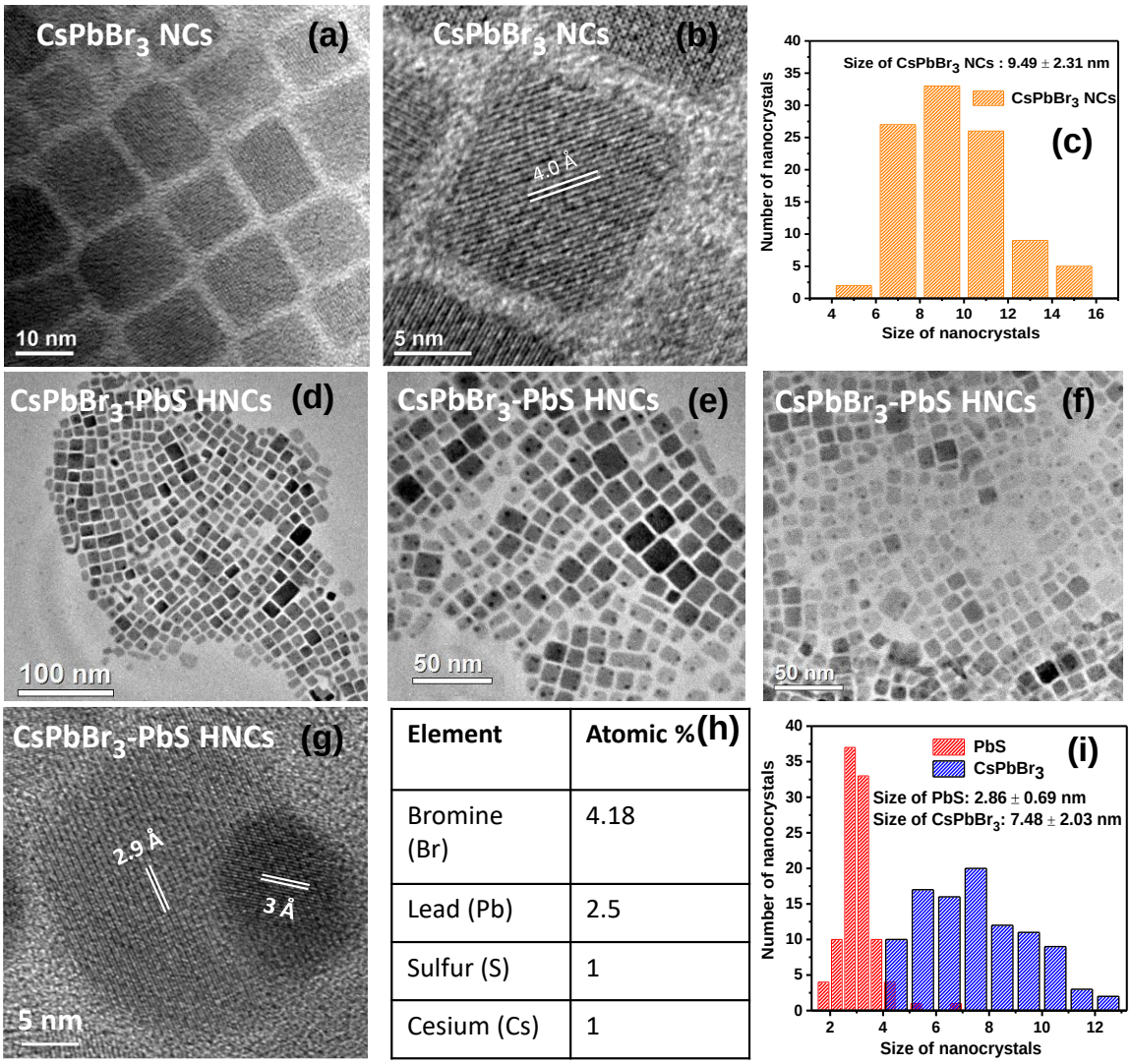

Element	Atomic % (h)
Bromine (Br)	4.18
Lead (Pb)	2.5
Sulfur (S)	1
Cesium (Cs)	1

Fig. 2 a) Transmission electron microscopy (TEM) image, b) high-resolution TEM (HRTEM) image, and c) size distribution plot of $CsPbBr_3$ NCs, respectively. d,e,f) TEM and g) HRTEM images of $CsPbBr_3$-PbS HNCs, respectively. h) energy-dispersive X-ray spectroscopy (EDS) analysis obtained from TEM image. i) size distribution plot of $CsPbBr_3$-PbS HNCs respectively. To get the size distribution plots, more than 100 NCs have been considered. To get the size of the $CsPbBr_3$ part in $CsPbBr_3$-PbS HNCs, the size of PbS has been measured in each NC and was subtracted from the size of corresponding $CsPbBr_3$-PbS HNCs.

Fig. 2d-f show TEM images of $CsPbBr_3$-PbS HNCs with the cubic morphology, indicating no change in the shape of the NC upon PbS incorporation. Each particle of HNCs contains one or more small black particles in the structure which was evident by TEM images (Fig. 2d-f). The black particles in the High-resolution TEM (HR-TEM) of the $CsPbBr_3$-PbS HNCs (Fig. 2g)

show an interplanar distance of 3.0 Å, confirming PbS (200) plane obtained in XRD spectra. Similarly, the interplanar distance of 2.9 Å corresponds to the (202) plane of $CsPbBr_3$ as observed in XRD. Energy-dispersive X-ray spectroscopy (EDS) carried out on the small dark, and the large light particles validate the formation of a heterostructure where PbS is embedded in the $CsPbBr_3$ NCs as shown in Fig. 2h. With a slight lattice mismatch (0.1Å) (202), planes of $CsPbBr_3$ are grown epitaxially on the plane (200) of PbS NCs, similar to the prior reports.[42, 47] Possible impurity phase formation under high electron beam intensities was also eliminated (Fig. S5). Simultaneously, we examined the TEM and EDS of $CsPbCl_3$-PbS and $CsPbI_3$-PbS HNCs as shown in Fig. S6 and Fig S7, further validating the formation of HNCs under the provided reaction conditions.

Our choice of synthesis conditions and resulting NCs can be understood by the nucleation and growth processes as described by La Mer's model. The thermal decomposition of lead and sulfur molecular precursors deliver the monomers of the PbS NCs. At the critical concentration, the nucleation takes place, leading to several atoms assembly to form a small thermodynamically stable PbS crystal. Concurrently, the ligands present in the solution which consists of amine and carboxylic acid functional groups bind to the metal ions on the surface while the alkyl group interacts with the reaction medium. Thus, the long alkyl chain controls the size of the crystals. Moreover, there is a dynamic equilibrium that occurs between the monomers and ligands during the growth process. Keeping longer reaction times lead to the making of larger crystals through Ostwald ripening. This Ostwald ripening process results in the broad size distribution of NCs. To avoid this, we use low concentration of sulfur precursor in our reaction. The concentration, reaction temperature, and ligand chemistry tuning results in smaller size PbS NCs. After the formation of PbS NCs, the temperature of the reaction mixture was raised and cesium precursor injected swiftly into the PbS NCs solution. The perovskite phase ($CsPbX_3$) started growing epitaxially on the surface of PbS NCs. The

schematic representation of $CsPbBr_3$ grown on PbS has shown in Fig. S8. The epitaxial growth of perovskite on the PbS surface is likely due to the coalescence of the perovskite octahedral ligand ($PbBr_6$) on the PbS surface. This lead to the adhering of neighbouring octahedral share edge and corner ions which results in the replacement of the outermost sulfur monolayer of PbS by halides, and the outermost Pb of PbS acts as an interface between PbS and $CsPbBr_3$ perovskite.[47-48] Further, theoretical studies of these heterostructures can give exact crystal structure of the interface similar to the other perovskite heterostructures.[37, 49-51]

TEM was also utilized to determine the size of the produced NCs, giving average diameters of 9.49±2.31 nm for the $CsPbBr_3$ NCs as shown in Fig. 2c and 7.48±2.03 nm and 2.86±0.69 nm for $CsPbBr_3$ and PbS respectively within the $CsPbBr_3$-PbS system, given in Fig. 2i. The reduced size of the $CsPbBr_3$ NCs within the heterostructure is likely due to the lower amount of Pb available for $CsPbBr_3$ formation. The synthesis of both $CsPbBr_3$ NCs and $CsPbBr_3$-PbS HNCs utilized the same initial amount of lead bromide precursor, but in the HNC reaction, a portion of the lead was consumed during the formation of PbS.

Multinuclear solid-state NMR was performed to further analyze the structure of the $CsPbBr_3$-PbS HNCs. The ^{207}Pb MAS NMR spectra of $CsPbBr_3$-PbS HNCs, $CsPbBr_3$ NCs, and PbS NCs are shown in Fig. 3a. NMR parameters obtained via spectral simulation are shown in Table S1in SI. The $CsPbBr_3$ NCs spectrum presents with a single ^{207}Pb line-shape at 260 ppm, which is perturbed by $J^1(^{207}Pb\text{-}^{79/81}Br)$ scalar coupling which produces a 19-spikelet splitting pattern. These results corroborate the previous reports[12, 52-53] of ^{207}Pb NMR on $CsPbBr_3$ crystal, which contains more in-depth discussions of the scalar coupling phenomena. The resolution of the scalar coupling pattern confirms the high level of crystallinity seen in the HRTEM images of the $CsPbBr_3$ NCs. The PbS NCs ^{207}Pb spectrum comprises one broad resonance at 1380 ppm, as expected from small nanoparticles (~3 nm diameter). To the best of our knowledge, this is the first published ^{207}Pb MAS NMR spectra of PbS, however, the chemical shift position is

corroborated by a previous unconfirmed report.[54] The ^{207}Pb NMR spectrum of the $CsPbBr_3$-PbS HNCs (Fig. 3a) contains resonances representing both the $CsPbBr_3$ and PbS NCs, with a $CsPbBr_3$:PbS ratio of around 3:1. Both resonances have shifted to lower frequencies and broadened in comparison to their pure NC analogs; the $CsPbBr_3$ resonance has broadened sufficiently to obscure its scalar coupling pattern. These changes to the NMR spectrum indicate distortion to the structure of the PbS and $CsPbBr_3$ NCs, suggesting that PbS incorporation has a wholesale effect on the perovskite chemical structure. Hence, ^{207}Pb NMR has confirmed the formation of a nanoscale heterostructure in the $CsPbBr_3$-PbS HNCs. ^{133}Cs MAS NMR was also utilized to investigate the structural differences between the $CsPbBr_3$ NCs and the $CsPbBr_3$-PbS HNCs. The ^{133}Cs spectra are shown in Fig. 3b and the NMR parameters are given in Table S2 in SI. The $CsPbBr_3$ NC spectrum is comprised of a sharp narrow resonance at 120 ppm, which represents the bulk $CsPbBr_3$, and multiple lower intensity, lower frequency "shoulder" resonances which represent the distorted surface/near-surface layers within the NC.

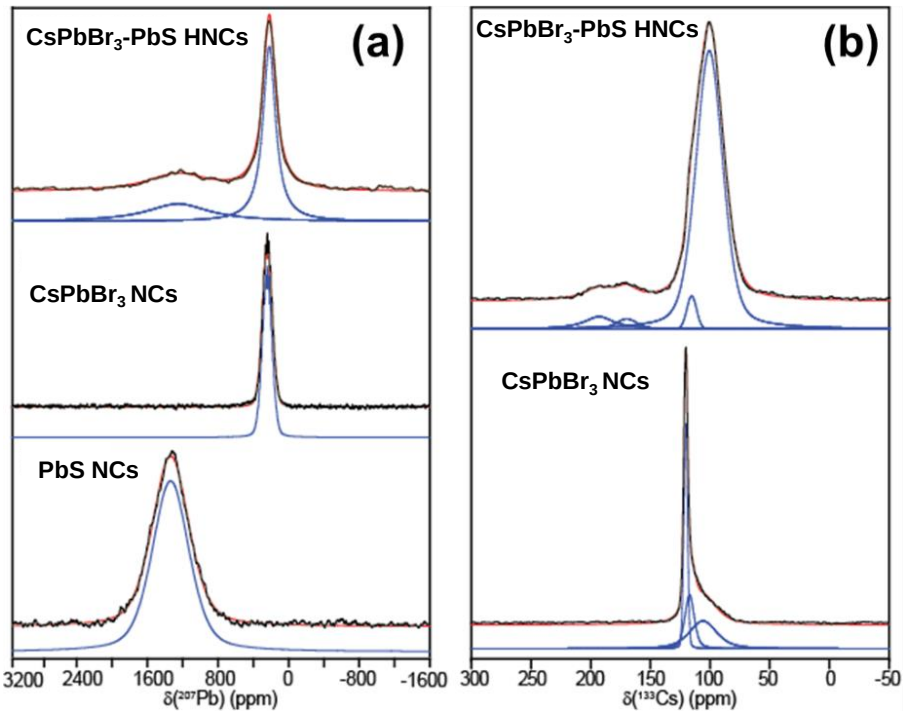

Fig. 3 a) ^{207}Pb MAS NMR of $CsPbBr_3$ NCs, PbS NCs and $CsPbBr_3$-PbS HNCs. b) ^{133}Cs MAS NMR of $CsPbBr_3$ NCs and $CsPbBr_3$-PbS HNCs. Experimental lines, simulated line-shapes, and deconvoluted resonances are represented by black, red, and blue lines respectively.

These results corroborate recent ^{133}Cs NMR studies of $CsPbBr_3$ NC systems, which are informed by similar bulk/surface effects seen in previous reports of ^{195}Pt and ^{105}Pd NMR of metallic nanoparticle systems.[12, 55-56] In the ^{133}Cs NMR spectrum of the $CsPbBr_3$-PbS HNCs, the dominant resonance at 102 ppm is broader and shifted than $CsPbBr_3$ NCs, analogously to the ^{207}Pb NMR data, confirming the distortion to the $CsPbBr_3$ NC structure due to PbS passivation. The reduction in average $CsPbBr_3$ particle diameter from the $CsPbBr_3$ NCs to the $CsPbBr_3$-PbS HNCs (from 9.5 to 7.5 nm) could explain a small portion of the distortion observed in the ^{133}Cs NMR due to the increased surface-to-bulk ratio of atoms in smaller particles. However, the difference in size is insufficient to explain the major broadening observed. A small resonance at 116 ppm is assigned as the unmodified $CsPbBr_3$ NCs in the system, which accounts for only 3% of the Cs nuclei, demonstrating the thorough passivation provided by this methodology. Additional resonances are observed in the ^{133}Cs NMR spectrum of $CsPbBr_3$-PbS at 193/170 ppm, which could represent Cs sites at the boundary between $CsPbBr_3$ and PbS.[54, 57]

Fig. 4a shows an optical absorption spectrum of $CsPbBr_3$ NCs and $CsPbBr_3$-PbS HNCs in the Ultraviolet-visible-NIR region. $CsPbBr_3$-PbS HNCs exhibit absorption in visible (450-520 nm) and to some extent to NIR visible region. The origin of absorption above 520 nm in HNCs can be attributed to PbS, which were embedded in each $CsPbBr_3$ particle. Characteristic emission in the green spectral region (513 nm) has been observed from both the $CsPbBr_3$ NCs and $CsPbBr_3$-PbS HNCs (Fig. 4b). Photoluminescence (PL) spectrum of $CsPbBr_3$-PbS HNCs shows a slightly higher energy shoulder probably due to the presence of smaller size $CsPbBr_3$ in $CsPbBr_3$-PbS HNCs sample as evident by Fig. 2i. Particularly, the inset of Fig. 4b shows the PL spectrum of $CsPbBr_3$-PbS HNCs in the NIR region similar to PbS NCs (Fig. S9a). Two PL peaks were observed at 800 nm and 850 nm upon excitation of 350 nm in agreement with the prior report.[58-61] These two peaks can be attributed to the band to band transition and defect-

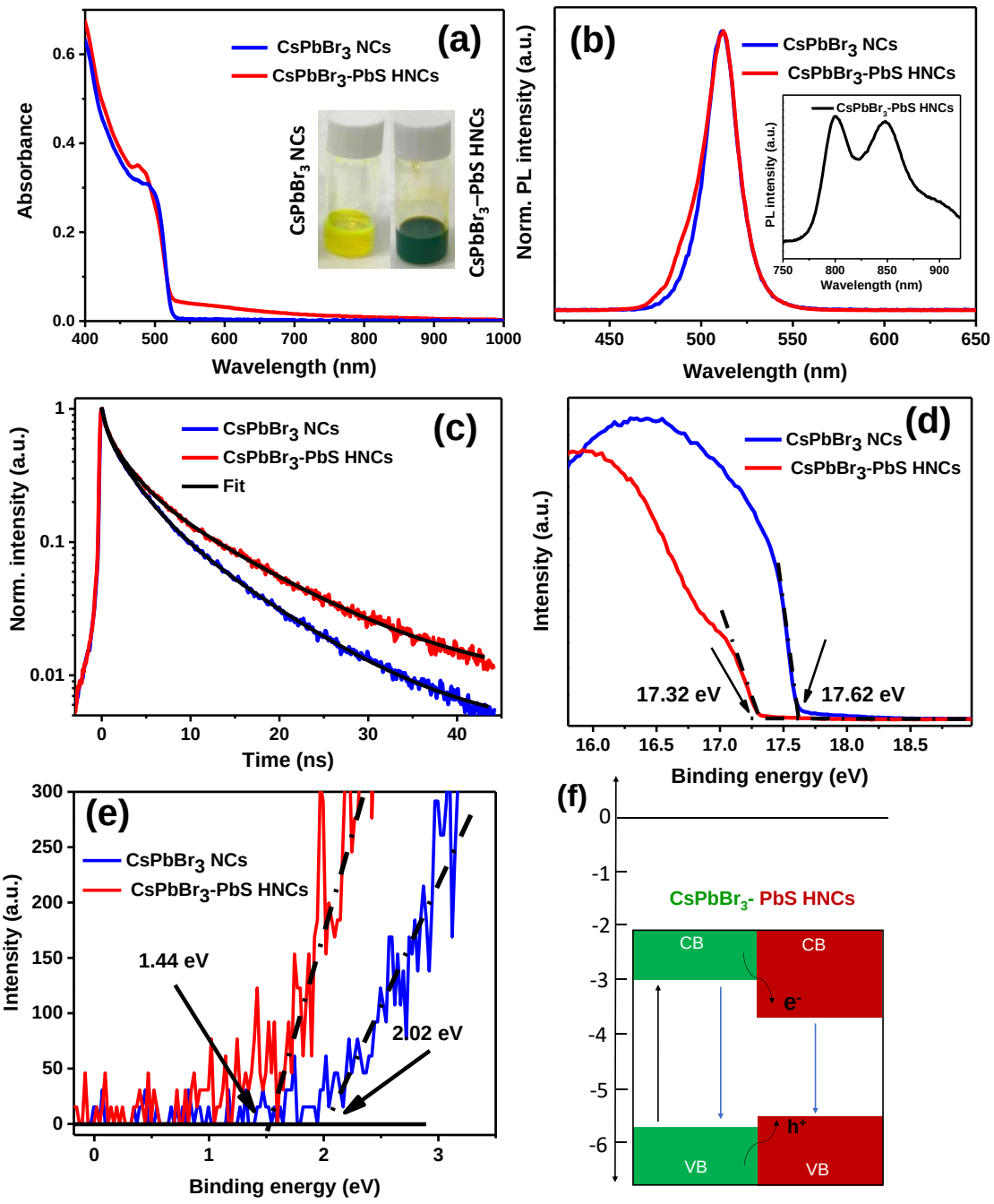

Fig. 4 a, b) absorption and photoluminescence (PL) of $CsPbBr_3$ NCs and $CsPbBr_3$-PbS HNCs, respectively. Inset of a) shows the photographs colloidal $CsPbBr_3$ NCs and $CsPbBr_3$-PbS HNCs under daylight. Inset of b) shows the PL of $CsPbBr_3$-PbS HNCs in the NIR region upon excitation at 350 nm. c) Time-resolved photoluminescence (TRPL) decay dynamics. d,e) Ultraviolet photoelectron spectroscopy (UPS) was carried out for $CsPbBr_3$-PbS HNCs in the cut-off region and valance region, respectively. f) Schematic representation of the band structure for $CsPbBr_3$-PbS HNCs at the interface. The exact VBM, CBM values have been given in Fig. S15.[62]

Table 1. Time resolved photoluminescence (TRPL) decay dynamics of $CsPbBr_3$ NCs and $CsPbBr_3$-PbS HNCs at 513 nm PL peak position. TRPL decay fitted using $I(t) = A_1 \exp(-t/\tau_1) + A_2 \exp(-t/\tau_2) + A_3 \exp(-t/\tau_3)$ equation, where A_1, A_2 and A_3 are the relative contributions and τ_1, τ_2 and τ_3 are the PL lifetime decay constants.

Type of NCs	A_1	τ_1 (ns)	A_2	τ_2 (ns)	A_3	τ_3 (ns)
$CsPbBr_3$ NCs	0.31 ±0.01	0.49±0.01	0.47±0.01	2.85±0.03	0.24±0.01	9.2±0.1
$CsPbBr_3$-PbS HNCs	0.25±0.01	0.50±0.01	0.43±0.01	2.59±0.06	0.30±0.01	10.7±0.2

related PL of PbS in the $CsPbBr_3$-PbS HNCs. To confirm the origin of NIR PL of $CsPbBr_3$-PbS HNCs, excitation spectra were collected at 800 nm and 850 nm as shown in Fig. S10a. Interestingly, the excitation spectra have a wide range of intensity from 450 to 700 nm. The shape of the excitation spectra resembles the absorption spectra of $CsPbBr_3$-PbS HNCs (Fig. S10b) and is distinctly different from the excitation spectra of PbS NCs as shown in Fig. S9b. This indicates energy/charge transfer from $CsPbBr_3$ to PbS. However, further investigation is needed to confirm the energy/charge transfer. On the other hand, absorption and PL in the NIR region are absent for $CsPbBr_3$ NCs as expected.

To understand the charge carrier dynamics of $CsPbBr_3$-PbS HNCs, time-resolved PL (TRPL) decay of $CsPbBr_3$ NCs and $CsPbBr_3$-PbS HNCs at their PL peak positions (in the visible region) were measured. Fig. 4c shows the TRPL of $CsPbBr_3$ NCs along with $CsPbBr_3$-PbS HNCs. The incorporation of PbS into $CsPbBr_3$ has made the PL decay slightly slower for $CsPbBr_3$-PbS HNCs. For best fit parameters, TRPL decay has been fitted by tri exponential decay using the equation: $I(t) = A_1 \exp(-t/\tau_1) + A_2 \exp(-t/\tau_2) + A_3 \exp(-t/\tau_3)$. Table 1 shows the detailed analysis of TRPL decay. The shortest PL lifetime component $\tau_1 \sim 0.5$ ns (sub-nanosecond lifetime) is the one that is most influenced by non-radiative processes.[63] This fast component (τ_1=0.5 ns) relative contribution (A_1) is also reduced from 0.31 to 0.25 suggests the decrease in trap state density for $CsPbBr_3$-PbS HNCs compared with $CsPbBr_3$ NCs (Table 1).

On the other hand, τ_2 and τ_3 corresponds to the radiative recombination of electron and hole. There was a negligible difference in the 2nd-lifetime component i.e. A_2 and τ_2, but for the third-lifetime component, the relative contribution A_3 and PL lifetime τ_3 increased from ~0.24 and 9.2 ns to 0.3 and ~10.7 ns respectively, suggesting the radiative decay is slower for $CsPbBr_3$-PbS HNCs compared with $CsPbBr_3$ NCs. The decrease in the relative contribution of non-radiative PL lifetime A_1 and increase in PL radiative lifetime components (τ_2 and τ_3) along with their relative contribution A_2 and A_3 of $CsPbBr_3$-PbS HNCs for $CsPbBr_3$ NCs should reflect in PL quantum yield (PLQY). The PLQYs of the samples were about ~ 20±2% and 30±3% for $CsPbBr_3$ NCs and $CsPbBr_3$-PbS HNCs respectively, which coincides with increased contribution from longer lifetime components of the TRPL as shown in table 1. The lower PLQY of NCs is due to the stripping of organic ligand (OLA/OA) upon washing of NCs with methyl acetate, which also agrees with the prior literature.[64] Details of the optical properties of $CsPbI_3$-PbS HNCs and $CsPbCl_3$-PbS HNCs have been discussed in Fig. S11 and S12 in the SI.

To investigate the band alignment of $CsPbBr_3$-PbS HNCs, UPS measurements have been carried out for $CsPbBr_3$ NCs, PbS NCs, and $CsPbBr_3$-PbS HNCs. The valence band maximum (VBM) has been calculated using the formula $E_{VBM} = 21.2\ eV - (E_{cutoff} - E_i)$, where 21.2 eV, E_{cutoff}, and E_i, correspond to ionization source (He I), kinetic cut-off energy, and Fermi energy, respectively.[65] The VBM of $CsPbBr_3$ NCs and $CsPbBr_3$-PbS HNCs have been calculated to be -5.6 eV and -5.32 eV as depicted in Fig. 4d,e. These values are in the agreement with the previous reports.[66-67] The corresponding conduction band minimum (CBM) was calculated using the optical bandgap, and the bandgap was extracted from the Tauc plot (Fig. S13). The VBM and CBM values for PbS NCs are about 5.45 eV and 3.85 eV (Fig. S14), respectively.[53] The band alignment of $CsPbBr_3$ NCs, PbS NCs, and $CsPbBr_3$-PbS HNCs is shown by the schematic in Fig. S15. The interface of $CsPbBr_3$ and PbS heterostructures is a type I band

alignment, as shown in Fig. 4f. The schematic in Fig. 4f explains the mechanism of electron-hole radiative recombination in $CsPbBr_3$-PbS HNCs, showing higher PL in the visible and NIR region in Fig. 4b. The PL results show that most electron-hole radiative recombination occurs in $CsPbBr_3$ is likely due to efficient delocalization between the VBM of $CsPbBr_3$ and PbS of $CsPbBr_3$-PbS HNCs (small energy difference, 0.13 eV) as shown in Fig. 4f and S15. Interestingly, PbS incorporation shifts Fermi values by 0.3 eV. This suggests the possibility of n-type to an ambipolar character for $CsPbBr_3$-PbS HNCs.[67] Often, type-I band alignment is desired for photomultiplication-assisted high-performance photodetector application.[68] On the other hand, the band alignment for $CsPbI_3$-PbS HNCs has been found out to be type-II (Fig. S18), which is helpful for charge separation in solar cell and multimodal neuromorphic synapse applications.[69]

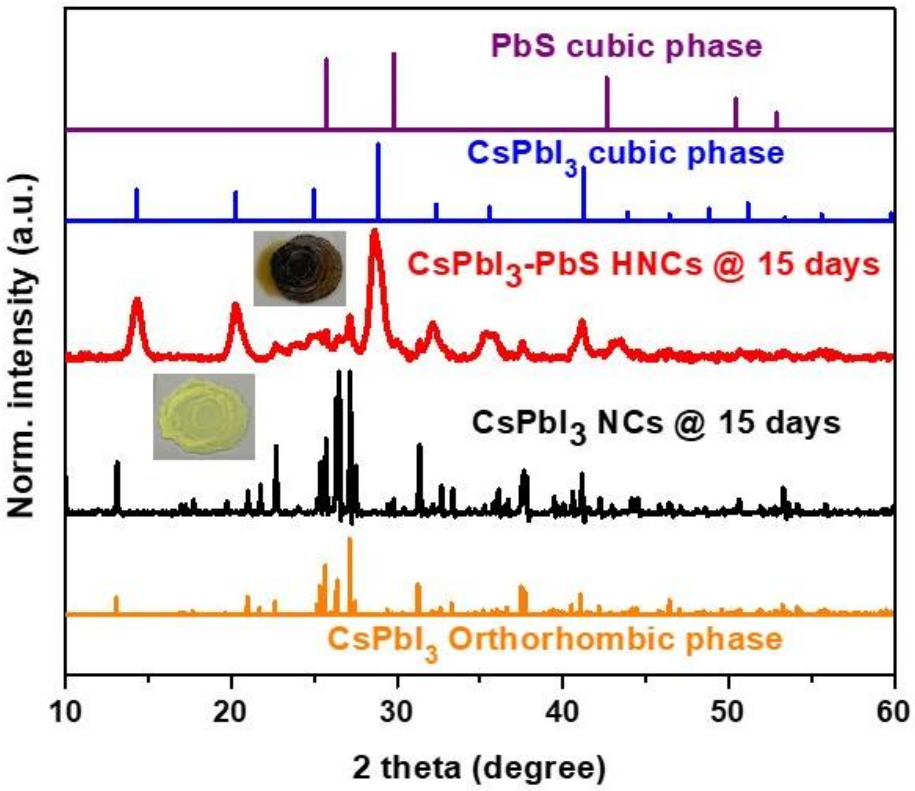

Fig. 5 XRD patterns of the films of $CsPbI_3$ NCs and $CsPbI_3$-PbS HNCs with time along with the reference pattern of $CsPbI_3$ and PbS. Inset shows the photograph of the films on the 15th day after making where yellow and brown color films correspond to $CsPbI_3$ NCs and $CsPbI_3$-PbS HNCs, respectively.

Finally, we examine $CsPbI_3$ cubic phase (black phase) stability upon PbS incorporation for its use in optoelectronic device applications. Thin films of $CsPbI_3$ NCs and $CsPbI_3$-PbS HNCs were made and tested over some time under ambient conditions. Figs. 5 and S18 depict stability of samples carried out under ambient conditions in which black $CsPbI_3$ NCs transform to yellow phase within five days. However, $CsPbI_3$-PbS HNCs films maintained their stability for the atleast 15 days as shown in Fig. 5. The complete conversion of cubic to the orthorhombic phase of our $CsPbI_3$-PbS HNCs would take more than 60 days (Fig. S19b). The enhanced stability can be attributed to the new chemical bonds and surfaces at the PbS- $CsPbI_3$ interface, and the small contribution of stress as shown by previous studies on PbS embedded $FAPbI_3$.[37] These combined effects lower the total energy of the cubic phase and make it more thermodynamically favourable in the PbS embedded $CsPbI_3$ NCs.[37] This significant enhancement of phase stability due to the embedding of PbS could allow the fabrication of perovskite NC-based stable optoelectronic devices without the assistance of a glovebox.

Typically, $CsPbBr_3$ which exists in the orthorhombic phase at room temperature shows superior stability as compared to $CsPbI_3$. However, we tested $CsPbBr_3$-PbS HNCs against polar solvent treatments, ambient testing, and UV light exposure upon inclusion of PbS in $CsPbBr_3$ NCs as shown in Fig. S20, S21, and S22 in SI. Interestingly, $CsPbBr_3$-PbS HNCs are more stable over $CsPbBr_3$ NCs. Thus, the embedding of PbS into $CsPbX_3$ NCs leads to new functional properties with enhanced stability. Finally, we also demonstrate scalability via larger-scale synthesis of $CsPbBr_3$-PbS HNCs and $CsPbI_3$-PbS HNCs as shown in Fig. S23.

Here, we have successfully demonstrated type-I ($CsPbBr_3$-PbS and $CsPbCl_3$-PbS) and type- II ($CsPbI_3$-PbS) HNCs prepared by the one-pot hot-injection method. The absorption and emission of $CsPbX_3$ NCs have been extended to the NIR region by embedding PbS NCs. We propose a unique synthesis protocol, which reduces synthesis time, steps and improves purity. Importantly, the syntheses of HNCs have been scaled up to a few hundred milligrams. We

believe this study limelight the possibility of the formation of HNCs such as perovskite/$CuInS_2$, Perovskite/ZnS, which will ultimately offer the advantages of both materials with higher stability.

Notes

The authors declare no competing financial interest.

ACKNOWLEDGMENTS

MJ would like to acknowledge the National Research Foundation, Prime Minister's Office, Singapore under its Competitive Research Programme (CRP Award No. NRF-CRP14-2014-03). We would like to acknowledge the Facility for Analysis, Characterization, Testing and Simulation, Nanyang Technological University, Singapore, for use of their electron microscopy/X-ray facilities. MJ acknowledge National Research Foundation of Korea (NRF) grant funded by the Korea government (MSIT) (No. 2020R1A4A1019455). PV acknowledges a Presidential Postdoctoral Fellowship from Nanyang Technological University (NTU), Singapore via grant 04INS000581C150. We would also like to acknowledge the NTU Centre of High Field NMR Spectroscopy and Imaging for the use of their NMR facilities. T.C.S and J.W.M.L acknowledge the financial support from the Singapore National Research Foundation through the NRF Investigatorship (NRF-NRFI-2018-04) and the Ministry of Education under its AcRF Tier 1 grant (RG91/19) and Tier 2 grant MOE2019-T2-1-006.

Supporting Information Available

Experimental details of the syntheses of $CsPbX_3$-PbS HNCs and $CsPbX_3$ NCs; characterization of NCs using UV-vis and PL spectroscopy; structural characterization by XRD, TEM, HRTEM, SEM; band alignment obtained from UPS; Photographs of the solutions of NCs; tables of ^{207}Pb and ^{133}Cs NMR parameters.

REFERENCES

(1). Hassan, Y.; Ashton, O. J.; Park, J. H.; Li, G.; Sakai, N.; Wenger, B.; Haghighirad, A.-A.; Noel, N. K.; Song, M. H.; Lee, B. R.; Friend, R. H.; Snaith, H. J., Facile Synthesis of

Stable and Highly Luminescent Methylammonium Lead Halide Nanocrystals for Efficient Light Emitting Devices. *J. Am. Chem. Soc.* **2019,** *141*, 1269-1279.

(2). Liang, H.; Yuan, F.; Johnston, A.; Gao, C.; Choubisa, H.; Gao, Y.; Wang, Y.-K.; Sagar, L. K.; Sun, B.; Li, P.; Bappi, G.; Chen, B.; Li, J.; Wang, Y.; Dong, Y.; Ma, D.; Gao, Y.; Liu, Y.; Yuan, M.; Saidaminov, M. I.; Hoogland, S.; Lu, Z.-H.; Sargent, E. H., High Color Purity Lead-Free Perovskite Light-Emitting Diodes via Sn Stabilization. *Adv. Sci.* **2020**, *7*, 1903213.

(3). Swarnkar, A.; Marshall, A. R.; Sanehira, E. M.; Chernomordik, B. D.; Moore, D. T.; Christians, J. A.; Chakrabarti, T.; Luther, J. M., Quantum Dot–Induced Phase Stabilization of α-$CsPbI_3$ Perovskite for High-Efficiency Photovoltaics. *Science* **2016,** *354*, 92-95.

(4). Wang, Y.; Dar, M. I.; Ono, L. K.; Zhang, T.; Kan, M.; Li, Y.; Zhang, L.; Wang, X.; Yang, Y.; Gao, X.; Qi, Y.; Grätzel, M.; Zhao, Y., Thermodynamically Stabilized β-$CsPbI_3$–Based Perovskite Solar Cells with Efficiencies >18%. *Science* **2019,** *365*, 591-595.

(5). Wu, C.; Wang, D.; Zhang, Y.; Gu, F.; Liu, G.; Zhu, N.; Luo, W.; Han, D.; Guo, X.; Qu, B.; Wang, S.; Bian, Z.; Chen, Z.; Xiao, L., $FAPbI_3$ Flexible Solar Cells with a Record Efficiency of 19.38% Fabricated in Air via Ligand and Additive Synergetic Process. *Adv. Funct. Mater.* **2019,** *29*, 1902974.

(6). Chin, X. Y.; Perumal, A.; Bruno, A.; Yantara, N.; Veldhuis, S. A.; Martínez-Sarti, L.; Chandran, B.; Chirvony, V.; Lo, A. S.-Z.; So, J.; Soci, C.; Grätzel, M.; Bolink, H. J.; Mathews, N.; Mhaisalkar, S. G., Self-Assembled Hierarchical Nanostructured Perovskites Enable Highly Efficient LEDs via an Energy Cascade. *Energy Environ. Sci.* **2018,** *11*, 1770-1778.

(7). Zhang, X.; Cao, W.; Wang, W.; Xu, B.; Liu, S.; Dai, H.; Chen, S.; Wang, K.; Sun, X. W., Efficient Light-Emitting Diodes Based on Green Perovskite Nanocrystals with Mixed-Metal Cations. *Nano Energy* **2016,** *30*, 511-516.

(8). Ramasamy, P.; Lim, D.-H.; Kim, B.; Lee, S.-H.; Lee, M.-S.; Lee, J.-S., All-Inorganic Cesium Lead Halide Perovskite Nanocrystals for Photodetector Applications. *Chem. Commun.* **2016,** *52*, 2067-2070.

(9). Cao, M.; Xu, Y.; Li, P.; Zhong, Q.; Yang, D.; Zhang, Q., Recent Advances and Perspectives on Light Emitting Diodes Fabricated from Halide Metal Perovskite Nanocrystals. *J. Mater. Chem. C* **2019,** *7*, 14412-14440.

(10). Fu, Y.; Zhu, H.; Schrader, A. W.; Liang, D.; Ding, Q.; Joshi, P.; Hwang, L.; Zhu, X. Y.; Jin, S., Nanowire Lasers of Formamidinium Lead Halide Perovskites and Their Stabilized Alloys with Improved Stability. *Nano Lett.* **2016,** *16*, 1000-1008.

(11). Manser, J. S.; Christians, J. A.; Kamat, P. V., Intriguing Optoelectronic Properties of Metal Halide Perovskites. *Chem. Rev.* **2016,** *116*, 12956-13008.

(12). Vashishtha, P.; Veldhuis, S. A.; Dintakurti, S. S. H.; Kelly, N. L.; Griffith, B. E.; Brown, A. A. M.; Ansari, M. S.; Bruno, A.; Mathews, N.; Fang, Y.; White, T.; Mhaisalkar, S. G.; Hanna, J. V., Investigating the Structure–Function Relationship in Triple Cation Perovskite Nanocrystals for Light-Emitting Diode Applications. *J. Mater. Chem. C* **2020**.

(13). Kulkarni, S. A.; Mhaisalkar, S. G.; Mathews, N.; Boix, P. P., Perovskite Nanoparticles: Synthesis, Properties, and Novel Applications in Photovoltaics and LEDs. *Small Methods* **2019,** *3*, 1800231.

(14). Shamsi, J.; Urban, A. S.; Imran, M.; De Trizio, L.; Manna, L., Metal Halide Perovskite Nanocrystals: Synthesis, Post-Synthesis Modifications, and Their Optical Properties. *Chem. Rev.* **2019,** *119*, 3296-3348.

(15). Vashishtha, P.; Bishnoi, S.; Li, C. H. A.; Jagadeeswararao, M.; Hooper, T. J. N.; Lohia, N.; Shivarudraiah, S. B.; Ansari, M. S.; Sharma, S. N.; Halpert, J. E. Recent Advancements in Near-Infrared Perovskite Light-Emitting Diodes. *ACS Appl. Electron. Mater.* **2020,** *2*, 3470-3490.

(16). Anaya, M.; Rubino, A.; Rojas, T. C.; Galisteo-López, J. F.; Calvo, M. E.; Míguez, H., Strong Quantum Confinement and Fast Photoemission Activation in $CH_3NH_3PbI_3$ Perovskite Nanocrystals Grown within Periodically Mesostructured Films. *Adv. Opt. Mater.* **2017,** *5*, 1601087.

(17). Sun, S.; Yuan, D.; Xu, Y.; Wang, A.; Deng, Z., Ligand-Mediated Synthesis of Shape-Controlled Cesium Lead Halide Perovskite Nanocrystals via Reprecipitation Process at Room Temperature. *ACS Nano* **2016,** *10*, 3648-3657.

(18). Ravi, V. K.; Markad, G. B.; Nag, A., Band Edge Energies and Excitonic Transition Probabilities of Colloidal $CsPbX_3$ (X = Cl, Br, I) Perovskite Nanocrystals. *ACS Energy Lett.* **2016,** *1*, 665-671.

(19). Ravi, V. K.; Swarnkar, A.; Chakraborty, R.; Nag, A., Excellent Green but Less Impressive Blue Luminescence from $CsPbBr_3$ Perovskite Nanocubes and Nanoplatelets. *Nanotechnology* **2016,** *27*, 325708.

(20). Cohen, T. A.; Milstein, T. J.; Kroupa, D. M.; MacKenzie, J. D.; Luscombe, C. K.; Gamelin, D. R., Quantum-Cutting Yb^{3+}-Doped Perovskite Nanocrystals for Monolithic Bilayer Luminescent Solar Concentrators. *J. Mater. Chem. A* **2019,** *7*, 9279-9288.

(21). Mir, W. J.; Jagadeeswararao, M.; Das, S.; Nag, A. Colloidal Mn-Doped Cesium Lead Halide Perovskite Nanoplatelets. *ACS Energy Lett.* **2017,** *2* , 537-543.

(22). Mir, W. J.; Mahor, Y.; Lohar, A.; Jagadeeswararao, M.; Das, S.; Mahamuni, S.; Nag, A. Postsynthesis Doping of Mn and Yb into $CsPbX_3$ (X = Cl, Br, or I) Perovskite Nanocrystals for Downconversion Emission. *Chem. Mater.* **2018,** *30*, 8170-8178.

(23). Kulbak, M.; Gupta, S.; Kedem, N.; Levine, I.; Bendikov, T.; Hodes, G.; Cahen, D., Cesium Enhances Long-Term Stability of Lead Bromide Perovskite-Based Solar Cells. *J. Phys. Chem. Lett.* **2016,** *7*, 167-172.

(24). Protesescu, L.; Yakunin, S.; Bodnarchuk, M. I.; Krieg, F.; Caputo, R.; Hendon, C. H.; Yang, R. X.; Walsh, A.; Kovalenko, M. V., Nanocrystals of Cesium Lead Halide Perovskites ($CsPbX_3$, X = Cl, Br, and I): Novel Optoelectronic Materials Showing Bright Emission with Wide Color Gamut. *Nano Lett.* **2015,** *15*, 3692-3696.

(25). Tamming, R. R.; Butkus, J.; Price, M. B.; Vashishtha, P.; Prasad, S. K. K.; Halpert, J. E.; Chen, K.; Hodgkiss, J. M., Ultrafast Spectrally Resolved Photoinduced Complex Refractive Index Changes in $CsPbBr_3$ Perovskites. *ACS Photonics* **2019,** *6*, 345-350.

(26). Huang, H.; Chen, B.; Wang, Z.; Hung, T. F.; Susha, A. S.; Zhong, H.; Rogach, A. L., Water Resistant $CsPbX_3$ Nanocrystals Coated with Polyhedral Oligomeric Silsesquioxane and Their Use as Solid State Luminophores in All-Perovskite White Light-Emitting Devices. *Chem. Sci* **2016,** *7*, 5699-5703.

(27). Wang, H.-C.; Lin, S.-Y.; Tang, A.-C.; Singh, B. P.; Tong, H.-C.; Chen, C.-Y.; Lee, Y.-C.; Tsai, T.-L.; Liu, R.-S., Mesoporous Silica Particles Integrated with All-Inorganic $CsPbBr_3$ Perovskite Quantum-Dot Nanocomposites (MP-PQDs) with High Stability and Wide Color Gamut Used for Backlight Display. *Angew. Chem.* **2016,** *55*, 7924-7929.

(28). Park, S.; Chang, W. J.; Lee, C. W.; Park, S.; Ahn, H.-Y.; Nam, K. T., Photocatalytic Hydrogen Generation from Hydriodic Acid Using Methylammonium Lead Iodide in Dynamic Equilibrium with Aqueous Solution. *Nat. Energy.* **2016,** *2*, 16185.

(29). Huang, S.; Li, Z.; Kong, L.; Zhu, N.; Shan, A.; Li, L. Enhancing the Stability of $CH_3NH_3PbBr_3$ Quantum Dots by Embedding in Silica Spheres Derived from Tetramethyl Orthosilicate in "Waterless" Toluene. *J. Am. Chem. Soc.* **2016,** *138*, 5749-5752.

(30). Li, Z.-J.; Hofman, E.; Li, J.; Davis, A. H.; Tung, C.-H.; Wu, L.-Z.; Zheng, W., Photoelectrochemically Active and Environmentally Stable $CsPbBr_3/TiO_2$ Core/Shell Nanocrystals. *Adv. Funct. Mater.* **2018,** *28*, 1704288.

(31). Xuan, T.; Huang, J.; Liu, H.; Lou, S.; Cao, L.; Gan, W.; Liu, R.-S.; Wang, J., Super-Hydrophobic Cesium Lead Halide Perovskite Quantum Dot-Polymer Composites with High Stability and Luminescent Efficiency for Wide Color Gamut White Light-Emitting Diodes. *Chem. Mater.* **2019,** *31*, 1042-1047.

(32). Li, Z.; Kong, L.; Huang, S.; Li, L. Highly Luminescent and Ultrastable $CsPbBr_3$ Perovskite Quantum Dots Incorporated into a Silica/Alumina Monolith. *Angew. Chem. Int. Ed.* **2017,** *56*, 8134-8138.

(33). Zhang, C.; Wang, B.; Li, W.; Huang, S.; Kong, L.; Li, Z.; Li, L., Conversion of Invisible Metal-Organic Frameworks to Luminescent Perovskite Nanocrystals for Confidential Information Encryption and Decryption. *Nat. Commun.* **2017,** *8*, 1138.

(34). Swarnkar, A.; Mir, W. J.; Nag, A. Can B-Site Doping or Alloying Improve Thermal- and Phase-Stability of All-Inorganic $CsPbX_3$ (X = Cl, Br, I) Perovskites? *ACS Energy Lett.* **2018,** *3*, 286-289.

(35). Mir, W. J.; Swarnkar, A.; Nag, A. Postsynthesis Mn-Doping in $CsPbI_3$ Nanocrystals to Stabilize the Black Perovskite Phase. *Nanoscale* **2019,** *11*, 4278-4286.

(36). Vashishtha, P.; Griffith, B. E.; Brown, A. A. M.; Hooper, T. J. N.; Fang, Y.; Ansari, M. S.; Bruno, A.; Pu, S. H.; Mhaisalkar, S. G.; White, T.; Hanna, J. V., Performance Enhanced Light-Emitting Diodes Fabricated from Nanocrystalline $CsPbBr_3$ with In Situ Zn^{2+} Addition. *ACS Appl. Electron. Mater.* **2020**, 2, 4002–4011

(37). Masi, S.; Echeverría-Arrondo, C.; Salim, K. M. M.; Ngo, T. T.; Mendez, P. F.; López-Fraguas, E.; Macias-Pinilla, D. F.; Planelles, J.; Climente, J. I.; Mora-Seró, I. Chemi-Structural Stabilization of Formamidinium Lead Iodide Perovskite by Using Embedded Quantum Dots. *ACS Energy Lett.* **2020,** *5*, 418-427.

(38). Zhang, T.; Ban, H.; Sun, Q.; Pan, H.; Yu, H.; Zhang, Z.; Zhang, X.; Shen, Y.; Wang, M. Preventing Inhomogeneous Elemental Distribution and Phase Segregation in Mixed Pb-Sn Inorganic Perovskites via Incorporating PbS Quantum Dots. *J. Energy Chem.* **2022,** *65*, 179-185.

(39). Wang, S.; Bi, C.; Portniagin, A.; Yuan, J.; Ning, J.; Xiao, X.; Zhang, X.; Li, Y. Y.; Kershaw, S. V.; Tian, J.; Rogach, A. L., $CsPbI_3$/PbSe Heterostructured Nanocrystals for High-Efficiency Solar Cells. *ACS Energy Lett.* **2020,** *5*, 2401-2410.

(40). Zhang, X.; Lu, M.; Zhang, Y.; Wu, H.; Shen, X.; Zhang, W.; Zheng, W.; Colvin, V. L.; Yu, W. W., PbS Capped $CsPbI_3$ Nanocrystals for Efficient and Stable Light-Emitting Devices Using p–i–n Structures. *ACS cent. sci.* **2018,** *4*, 1352-1359.

(41). Ma, Y.; Vashishtha, P.; Shivarudraiah, S. B.; Chen, K.; Liu, Y.; Hodgkiss, J. M.; Halpert, J. E., A Hybrid Perovskite Solar Cell Modified with Copper Indium Sulfide Nanocrystals to Enhance Hole Transport and Moisture Stability. *Solar RRL* **2017,** *1*, 1700078.

(42). Ning, Z.; Gong, X.; Comin, R.; Walters, G.; Fan, F.; Voznyy, O.; Yassitepe, E.; Buin, A.; Hoogland, S.; Sargent, E. H. Quantum-Dot-in-Perovskite Solids. *Nature* **2015,** *523*, 324-328.

(43). Liu, M.; Chen, Y.; Tan, C.-S.; Quintero-Bermudez, R.; Proppe, A. H.; Munir, R.; Tan, H.; Voznyy, O.; Scheffel, B.; Walters, G.; Kam, A. P. T.; Sun, B.; Choi, M.-J.; Hoogland, S.; Amassian, A.; Kelley, S. O.; García de Arquer, F. P.; Sargent, E. H. Lattice Anchoring Stabilizes Solution-Processed Semiconductors. *Nature* **2019,** *570*, 96-101.

(44). Gaulding, E. A.; Chen, X.; Yang, Y.; Harvey, S. P.; To, B.; Kim, Y.-H.; Beard, M. C.; Sercel, P. C.; Luther, J. M. Embedding PbS Quantum Dots (QDs) in Pb-Halide Perovskite Matrices: QD Surface Chemistry and Antisolvent Effects on QD Dispersion and Confinement Properties. *ACS Mater. Lett.* **2020,** *2*, 1464-1472.

(45). Zhang, X.; Wu, X.; Liu, X.; Chen, G.; Wang, Y.; Bao, J.; Xu, X.; Liu, X.; Zhang, Q.; Yu, K., Heterostructural $CsPbX_3$-PbS (X= Cl, Br, I) Quantum Dots with Tunable Vis–NIR Dual Emission. *J. Am. Chem. Soc.* **2020,** *142*, 4464-4471.

(46). Liu, H.; Tan, Y.; Cao, M.; Hu, H.; Wu, L.; Yu, X.; Wang, L.; Sun, B.; Zhang, Q., Fabricating $CsPbX_3$-Based Type I and Type II Heterostructures by Tuning the Halide Composition of Janus $CsPbX_3/ZrO_2$ Nanocrystals. *ACS Nano* **2019,** *13*, 5366-5374.

(47). Zhang, X.; Zhang, J.; Phuyal, D.; Du, J.; Tian, L.; Öberg, V. A.; Johansson, M. B.; Cappel, U. B.; Karis, O.; Liu, J.; Rensmo, H.; Boschloo, G.; Johansson, E. M. J. Inorganic $CsPbI_3$ Perovskite Coating on PbS Quantum Dot for Highly Efficient and Stable Infrared Light Converting Solar Cells. *Adv. Energy Mater.* **2018,** *8*, 1702049.

(48). Sytnyk, M.; Yakunin, S.; Schöfberger, W.; Lechner, R. T.; Burian, M.; Ludescher, L.; Killilea, N. A.; YousefiAmin, A.; Kriegner, D.; Stangl, J.; Groiss, H.; Heiss, W. Quasi-Epitaxial Metal-Halide Perovskite Ligand Shells on PbS Nanocrystals. *ACS Nano* **2017,** *11*, 1246-1256.

(49). Tang, X.; Yang, J.; Li, S.; Liu, Z.; Hu, Z.; Hao, J.; Du, J.; Leng, Y.; Qin, H.; Lin, X.; Lin, Y.; Tian, Y.; Zhou, M.; Xiong, Q. Single Halide Perovskite/Semiconductor Core/Shell Quantum Dots with Ultrastability and Nonblinking Properties. *Adv. Sci.* **2019,** *6*, 1900412.

(50). Pan, L.-Y.; Ding, Y.-F.; Yu, Z.-L.; Wan, Q.; Liu, B.; Cai, M.-Q. Layer-Dependent Optoelectronic Property for All-Inorganic Two-Dimensional Mixed Halide Perovskite $Cs_2PbI_2Cl_2$ with a Ruddlesden-Popper Structure. *J. Power Sources* **2020,** *451*, 227732.

(51). Liu, B.; Long, M.; Cai, M.-Q.; Yang, J. Two-Dimensional Van Der Waals Heterostructures Constructed via Perovskite $(C_4H_9NH_3)_2XBr_4$ and Black Phosphorus. *J. Phys. Chem. Lett.* **2018,** *9*, 4822-4827.

(52). Aebli, M.; Piveteau, L.; Nazarenko, O.; Benin, B. M.; Krieg, F.; Verel, R.; Kovalenko, M. V., Lead-Halide Scalar Couplings in ^{207}Pb NMR of $APbX_3$ Perovskites (A = Cs, Methylammonium, Formamidinium; X = Cl, Br, I). *Sci. Rep.* **2020,** *10*, 8229.

(53). Ray, A.; Maggioni, D.; Baranov, D.; Dang, Z.; Prato, M.; Akkerman, Q. A.; Goldoni, L.; Caneva, E.; Manna, L.; Abdelhady, A. L., Green-Emitting Powders of Zero-Dimensional Cs_4PbBr_6: Delineating the Intricacies of the Synthesis and the Origin of Photoluminescence. *Chem. Mater.* **2019,** *31*, 7761-7769.

(54). Neue, G.; Dybowski, C.; Smith, M. L.; Hepp, M. A.; Perry, D. L., Determination of $^{207}Pb^{2+}$ Chemical Shift Tensors from Precise Powder Lineshape Analysis. *Solid State Nucl. Magn. Reson.* **1996,** *6*, 241-250.

(55). Rees, G. J.; Orr, S. T.; Barrett, L. O.; Fisher, J. M.; Houghton, J.; Spikes, G. H.; Theobald, B. R. C.; Thompsett, D.; Smith, M. E.; Hanna, J. V., Characterisation of Platinum-Based Fuel Cell Catalyst Materials Using ^{195}Pt Wideline Solid State NMR. *Phys. Chem. Chem. Phys.* **2013,** *15*, 17195-17207.

(56). Hooper, T. J. N.; Partridge, T. A.; Rees, G. J.; Keeble, D. S.; Powell, N. A.; Smith, M. E.; Mikheenko, I. P.; Macaskie, L. E.; Bishop, P. T.; Hanna, J. V., Direct Solid State NMR Observation of the ^{105}Pd Nucleus in Inorganic Compounds and Palladium Metal Systems. *Phys. Chem. Chem. Phys.* **2018,** *20*, 26734-26743.

(57). Chen, Y.; Smock, S. R.; Flintgruber, A. H.; Perras, F. A.; Brutchey, R. L.; Rossini, A. J., Surface Termination of $CsPbBr_3$ Perovskite Quantum Dots Determined by Solid-State NMR Spectroscopy. *J. Am. Chem. Soc.* **2020,** *142*, 6117-6127.

(58). Binetti, E.; Striccoli, M.; Sibillano, T.; Giannini, C.; Brescia, R.; Falqui, A.; Comparelli, R.; Corricelli, M.; Tommasi, R.; Agostiano, A.; Curri, M. L., Tuning Light Emission of PbS Nanocrystals from Infrared to Visible Range by Cation Exchange. *Sci Technol Adv Mater* **2015,** *16*, 055007-055007.

(59). Zhao, X.; Gorelikov, I.; Musikhin, S.; Cauchi, S.; Sukhovatkin, V.; Sargent, E. H.; Kumacheva, E., Synthesis and Optical Properties of Thiol-Stabilized PbS Nanocrystals. *Langmuir* **2005,** *21*, 1086-1090.

(60). Hines, M. A.; Scholes, G. D., Colloidal PbS Nanocrystals with Size-Tunable Near-Infrared Emission: Observation of Post-Synthesis Self-Narrowing of the Particle Size Distribution. *Adv. Mater.* **2003,** *15*, 1844-1849.

(61). Nordin, M.; Li, J.; Clowes, S.; Curry, R., Temperature Dependent Optical Properties of PbS Nanocrystals. *Nanotechnology* **2012,** *23*, 275701.

(62). Wang, Y.; Liu, Z.; Huo, N.; Li, F.; Gu, M.; Ling, X.; Zhang, Y.; Lu, K.; Han, L.; Fang, H.; Shulga, A. G.; Xue, Y.; Zhou, S.; Yang, F.; Tang, X.; Zheng, J.; Antonietta Loi, M.; Konstantatos, G.; Ma, W., Room-Temperature Direct Synthesis of Semi-Conductive PbS Nanocrystal Inks for Optoelectronic Applications. *Nat. Commun.* **2019,** *10*, 5136.

(63). Rao, M. J.; Shibata, T.; Chattopadhyay, S.; Nag, A., Origin of Photoluminescence and XAFS Study of $(ZnS)_{1-x}(AgInS_2)_x$ Nanocrystals. *J. Phys. Chem. Lett.* **2014,** *5*, 167-173.

(64). Krieg, F.; Ochsenbein, S. T.; Yakunin, S.; ten Brinck, S.; Aellen, P.; Süess, A.; Clerc, B.; Guggisberg, D.; Nazarenko, O.; Shynkarenko, Y.; Kumar, S.; Shih, C.-J.; Infante, I.; Kovalenko, M. V., Colloidal $CsPbX_3$ (X = Cl, Br, I) Nanocrystals 2.0: Zwitterionic Capping Ligands for Improved Durability and Stability. *ACS Energy Lett.* **2018,** *3*, 641-646.

(65). Ji, L.; Zhang, X.; Zhang, T.; Wang, Y.; Wang, F.; Zhong, Z.; Chen, Z. D.; Xiao, Z.; Chen, L.; Li, S., Band Alignment of Pb–Sn Mixed Triple Cation Perovskites for Inverted Solar Cells with Negligible Hysteresis. *J. Mater. Chem. A* **2019,** *7*, 9154-9162.

(66). Ding, C.; Zhang, Y.; Liu, F.; Nakazawa, N.; Huang, Q.; Hayase, S.; Ogomi, Y.; Toyoda, T.; Wang, R.; Shen, Q., Recombination Suppression in PbS Quantum Dot Heterojunction Solar Cells by Energy-Level Alignment in the Quantum Dot Active Layers. *ACS Appl. Mater. Interfaces* **2018,** *10*, 26142-26152.

(67). Pan, J.; Quan, L. N.; Zhao, Y.; Peng, W.; Murali, B.; Sarmah, S. P.; Yuan, M.; Sinatra, L.; Alyami, N. M.; Liu, J.; Yassitepe, E.; Yang, Z.; Voznyy, O.; Comin, R.; Hedhili, M. N.; Mohammed, O. F.; Lu, Z. H.; Kim, D. H.; Sargent, E. H.; Bakr, O. M., Highly Efficient Perovskite-Quantum-Dot Light-Emitting Diodes by Surface Engineering. *Adv. Mater.* **2016,** *28*, 8718-8725.

(68). Liu, C.; Peng, H.; Wang, K.; Wei, C.; Wang, Z.; Gong, X. PbS Quantum Dots-Induced Trap-Assisted Charge Injection in Perovskite Photodetectors. *Nano Energy* **2016,** *30*, 27-35.

(69). Subramanian Periyal, S.; Jagadeeswararao, M.; Ng, S. E.; John, R. A.; Mathews, N. Halide Perovskite Quantum Dots Photosensitized-Amorphous Oxide Transistors for Multimodal Synapses. *Adv. Mater. Technol.* **2020,** *5*, 2000514.

Supporting information (SI)

Chemicals

Lead bromide (99.5%), lead iodide (99.999%), lead chloride (99.999%), cesium carbonate (99.9%), thioacetamide (≥99.0%), 1-octadecene (90%), oleylamine (70%), trioctylphosphine (97%), oleic acid (90%), methyl acetate (anhydrous, 99.5%), hexane (anhydrous, 95%) were purchased from Sigma-Aldrich and used as such unless until mentioned further purification.

Experimental section

Cs-oleate preparation

134.4 mg of cesium carbonate was loaded in a 3-neck round bottom flask along with 5 mL 1-octadecene and 1 mL oleic acid, degassed for 1 hour at 100 ^{o}C followed by shifted to nitrogen (N_2) environment then the temperature was raised to 150 ^{o}C to make sure cesium carbonate get dissolved completely. After that natural cooling to room temperature (RT).

Synthesis of $CsPbX_3$-PbS heterostructure nanocrystals (HNCs)

To synthesize $CsPbBr_3$-PbS HNCs, 0.19 mmol (~ 70 mg) of lead bromide was loaded in a 3-neck round bottom flask containing 5 mL 1-octadecene and this mixture was degassed for 1 hour at 100 °C. After which, the reaction flask was switched to the N_2 environment followed by the injection of 0.30 mL of dried oleylamine (OLA) and 0.55 mL dried oleic acid. This reaction mixture was degassed for another 15 minutes at 100 ^{o}C under vacuum and then finally switched back to the N_2 environment. The temperature of the lead bromide solution was then raised to 135 °C for dropwise addition of thioacetamide solution containing 5% (4 mg) of thioacetamide dissolved in 0.25 mL of dried OLA. This addition results in a color change of reaction mixture from colorless to a dark brown color solution. Subsequently, the temperature of the solution was further raised to 160 °C, then 0.5 mL Cs-oleate (which was heated up to 80-100 ^{o}C before injection) was injected swiftly, after 5-8 sec, the reaction flask was cooled down in an ice-water bath. After Cs-oleate injection the color of the solution turns black greenish as shown in Figure S1a. The reaction mixture was kept at RT for 15 minutes then the solution was centrifuged for 8000 rpm for 5 minutes and collected the decant was dispersed in 1 mL anhydrous hexane. To this, 1 mL methyl acetate (MeOAc) was added and again the mixture was centrifuged for 5 min at 8000 rpm, the resulting precipitate was collected. The

final precipitate was then dispersed in 1 mL hexane for further characterization. To make 2%, 1.2 mg of thioacetamide was dissolved in 0.25 mL dried OLA. The remaining procedure was the same as 5% reaction. To synthesize $CsPbI_3$-PbS and $CsPbCl_3$-PbS HNCs 0.19 mmol of PbI_2 and $PbCl_2$ were used. Additionally, 1 mL trioctylphosphine (TOP) was added to $PbCl_2$ solution. The remaining procedure is similar to the synthesis of $CsPbBr_3$-PbS HNCs.

Large scale synthesis of $CsPbBr_3$-PbS and $CsPbI_3$-PbS HNCs:

2.1 mmol of $PbBr_2$ has been taken in a 500 mL round bottom flask which contains 50 mL 1-octadecene. This mixture was degassed for 30 minutes to one hour at 100 ^oC followed by the injection of 5 mL OA and 4 mL OLA under N_2 environment. Again, the above reaction mixture was degassed at 100 ^oC and 110 ^oC for 30 minutes. After degassing 1 mL of the sulfur precursor was injected dropwise at 135 ^oC under N_2 environment. A sulfur precursor was prepared by dissolving ~ 0.5 mmol thioacetamide in 1 mL OLA by sonication. After that, the reaction temperature has been raised to 160 ^oC. At this temperature, 4 mL of Cs-oleate (which was heated to 80 ^oC before injection) was swiftly injected, after 5-8 sec, the reaction flask was cooled down in an ice-water bath until the solution becomes completely freezes. This NC solution allowed to reach RT. Then, this solution has been divided into eight parts in 50 ml centrifugation tubes. To each tube, 24 mL of MeOAc was added followed by centrifugation at 8000 rpm for 5 minutes. The resultant wet pellet was dispersed in 3 mL of hexane. To this 6 mL of MeOAc was added followed by centrifugation at 10000 rpm for 5 minutes. The final wet pellet was dispersed in 10 mL hexane. Larger size NCs have been removed by the centrifugation at 4000 rpm for 5 min.[1]

Synthesis of $CsPbX_3$ NCs

Synthesis of $CsPbBr_3$ NCs is similar to $CsPbBr_3$-PbS HNCs, since the sulfur source is not needed in this case, 0.55 mL dried OLA was added to lead bromide solution along with 0.55 mL OA. The remaining the procedure is same for both $CsPbBr_3$ NCs and $CsPbBr_3$-PbS HNCs. To synthesize $CsPbI_3$ and $CsPbCl_3$ NCs PbI_2 and $PbCl_2$ were used respectively. Additionally, 1 mL TOP was used to dissolve $PbCl_2$. The remaining procedure is similar to the synthesis of $CsPbBr_3$ NCs.

Synthesis of PbS NCs from $PbBr_2$, PbI_2, and $PbCl_2$ sources

To synthesize PbS NCs from $PbBr_2$, PbI_2, and $PbCl_2$ sources 5% of thioacetamide was added to $PbBr_2$, PbI_2, and $PbCl_2$ solution as described in the synthesis of $CsPbBr_3$-PbS, $CsPbI_3$-PbS,

and $CsPbCl_3$-PbS HNCs respectively, for about one minute followed by sudden cooling by an ice water bath. PbS NCs were purified by excess MeOAc solvent and centrifuged at 8000 rpm for 5 minutes to collect the precipitate. The obtained precipitate was dispersed in 1 mL hexane solvent. These PbS NCs were washed one more time with a 1:1 ratio of MeOAc. The final precipitate was dispersed in hexane for further characterization. In the manuscript, the PbS NCS from different halide sources have been represented by PbS NCs@$PbBr_2$, PbS NCs@ $PbCl_2$, and PbS NCs@PbI_2.

Characterization

UV-visible-NIR absorption and PL spectra were collected using Shimatzu and Horiba instruments, respectively. A small amount of NCs was dispersed in a quartz cuvette containing ~ 3 mL hexane for UV and PL measurements. XRD measurement of $CsPbBr_3$-PbS HNCs, PbS NCs@$PbBr_2$ and $CsPbBr_3$ NCs were conducted using a PANalytical X-ray diffractometer equipped with a 1.8kW Cu Kα X-ray tube and operating at 45 kV and 30 mA. The diffraction patterns were collected in the air at room temperature using Bragg-Brentano geometry. $CsPbCl_3$ NCs, $CsPbI_3$ NCs and $CsPbCl_3$-PbS, $CsPbI_3$-PbS HNCs XRD were collected using Bruker D8 Advance x-ray diffractometer using Cu Kα radiation (1.54 Å). All XRD samples were prepared by drop-casting a concentrated solution on a zero-diffraction silicon holder unless until mentioned. For Ultraviolet photoelectron spectroscopy (UPS) measurements for $CsPbBr_3$-PbS HNCs, PbS NCs from $PbBr_2$ source and $CsPbBr_3$ NCs solution was drop cast on ITO substrates. Whereas, samples correspond to PbS NCs @ PbI_2, $CsPbI_3$ NCs and $CsPbI_3$-PbS were done on silicon wafer. High-resolution transmission electron microscopy (HRTEM) measurements of $CsPbBr_3$ NCs and $CsPbBr_3$-PbS HNCs were performed by Jeol 2100F. The measurements were carried out with a beam current of 146 μA and an accelerating voltage of 200 kV. TEM measurements of $CsPbCl_3$ NCs, $CsPbI_3$ NCs and $CsPbCl_3$-PbS, $CsPbI_3$-PbS HNCs were measured using JEM-ARM. Samples were prepared by drop-casting diluted NCs solution (in hexane) onto the Cu grid. Fourier Transform Infrared Spectroscopy (FTIR) analyses were carried out using VERTEX 70v FT-IR spectrometer for the colloidal dispersion in hexane solvent. S-4800 from Hitachi Scanning electron microscope (SEM) have utilized for the measurement of energy dispersive spectroscopy (**EDS**) analysis for $CsPbCl_3$-PbS, $CsPbI_3$-PbS HNCs.

Time-resolved photoluminescence measurement

Time-resolved photoluminescence (TRPL) measurements were performed using a home-built setup. The excitation laser is a *Coherent LIBRA*, with a pulse duration of ~50 fs and a repetition rate of 1 kHz. The 400 nm pump beam was generated from frequency doubling the 800 nm fundamental beam using a BBO crystal. The residual 800 nm beam was filtered out with appropriate filters after frequency doubling. The photoluminescence was collected with a lens pair and directed into a monochromator (*Princeton Instrument SP2300i*) which was coupled to the streak camera (*Optronis Optoscope*) for measurement. The pump fluence used for the TRPL measurements was 4.5 μJcm^{-2}.

Photoluminescence quantum yield (PL QY) measurements

PL QY measurements have been carried out by exciting the samples with a 445 nm continuous-wave diode laser (Cobolt) in an integrating sphere (Labsphere). The output of the integrating sphere is coupled through an optical fiber to a charge-coupled device (Newton 920 CCD, Andor) in which the photon count is captured. Samples were prepared by taking the dilute solutions of nanocrystals in hexane solvent with absorbance ~ 0.2.

UPS measurements:

X-ray photoelectron spectroscopy (XPS) depth profiling was performed using an AXIS Supra spectrometer (Kratos Analytical Inc., UK) equipped with a hemispherical analyzer and a monochromatic Al K-alpha source (1487 eV) operated at 15 mA and 15 kV. The etching was done with an Ar Gas Cluster Ion Source (GCIS, Kratos Analytical Inc., Minibeam 6) operated at 10 keV, Ar1000+ with a roster size of 2 x 2 mm2. The high-resolution XPS spectra were acquired from an area of 700 x 300 μm2 after 60-s etch for each cycle. The sample was electrically grounded to the sample holder to prevent charge build-up on the sample surface. This instrument has used for $CsPbBr_3$ NCs and $CsPbBr_3$-PbS HNCs. UPS measurements of $CsPbCl_3$ NCs, $CsPbI_3$ NCs, and $CsPbCl_3$-PbS, $CsPbI_3$-PbS HNCs were measured in an ultrahigh-vacuum chamber with a 4D beamline equipped with an electron analyzer and heating element, at the Pohang Acceleration Laboratory. Results were corrected for charging effects using an Au internal reference.

Solid-state NMR measurements

All-solid-state NMR experiments in this study were completed on a 14.1 T Bruker Advance III HD 600 MHz spectrometer with a Bruker 1.9mm HXY MAS probe operating at a MAS

frequency of 24 kHz. The ^{133}Cs NMR (ν_0(^{133}Cs) = 78.729 MHz) experiments employed a one-pulse sequence, utilizing a selective $\pi/2$ pulse of 6.5 μs (determined on $CsCl_{(s)}$) and a recycle delay of 30-200 s. The resulting data was referenced with respect to 0.1 M $CsNO_{3(aq)}$ (δ_{iso} = 0 ppm). The ^{207}Pb NMR (ν_0(^{207}Pb) = 125.745-125.595 MHz) experiments employed a Hahn-echo pulse sequence, utilizing $\pi/2$ and π pulses of 4.125 and 8.25 μs (determined on 1.1 M $Pb(NO_3)_{2(aq)}$), a recycle delay of 1-2 s, and a rotor synchronized echo delay of 35.5 μs. The ^{207}Pb experiments utilized variable offset cumulative spectroscopy (VOCs) frequency stepping where appropriate to allow for full excitation of the broader NMR line-shapes present in some of the spectra. The resulting data were referenced with respect to 1.1 M $Pb(NO_3)_{2(aq)}$ (δ_{iso} = −2965.7 ppm). All spectral simulation was performed using the DMFit software package.[2]

Stability checking of $CsPbBr_3$-PbS HNCs:

Typically, $CsPbBr_3$ NCs having cubic and orthorhombic phases show high photoluminescence quantum yield (PLQY) unlike the orthorhombic phase of $CsPbI_3$ NCs. Therefore, phase stability is not studied for $CsPbBr_3$-PbS HNCs rather polar solvent treatment, ambient stability, and UV light exposure was studied for $CsPbBr_3$-PbS HNCs and $CsPbBr_3$ NCs. Fig. S19 shows the PL intensity change of ethanol treatment for 2 hours. Interestingly, $CsPbBr_3$-PbS HNCs exhibits better stability compared with $CsPbBr_3$ NCs. On the other hand, films of $CsPbBr_3$ NCs and $CsPbBr_3$-PbS HNCs show similar stability towards ambient and UV light exposure (Fig. S20 and S21). Therefore, with a broad absorption range from 400 nm to 750 nm with type I band alignment, less trap state density, and better stability, $CsPbBr_3$-PbS HNCs can be a potential candidate for photocatalysis, photomultiplication, and other optoelectronic applications.

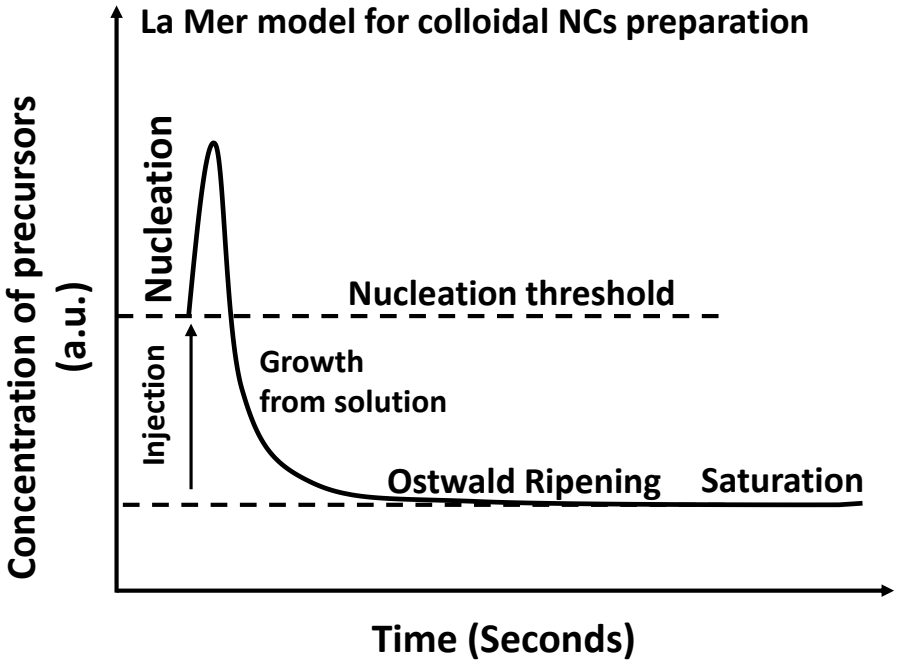

Fig. S1 La Mer model for preparing monodisperse colloidal nanocrystals.[3]

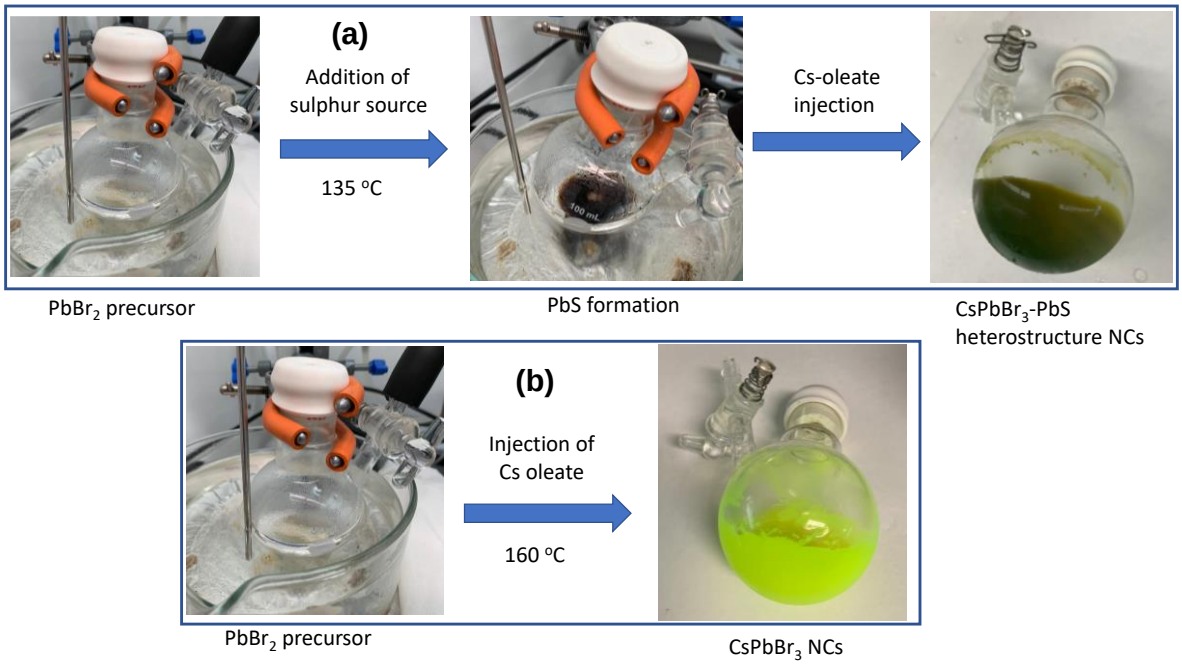

Fig. S2 a) and b) are showing the photographs of the formation of $CsPbBr_3$-PbS heterostructure nanocrystals (HNCs) and $CsPbBr_3$ nanocrystals (NCs).

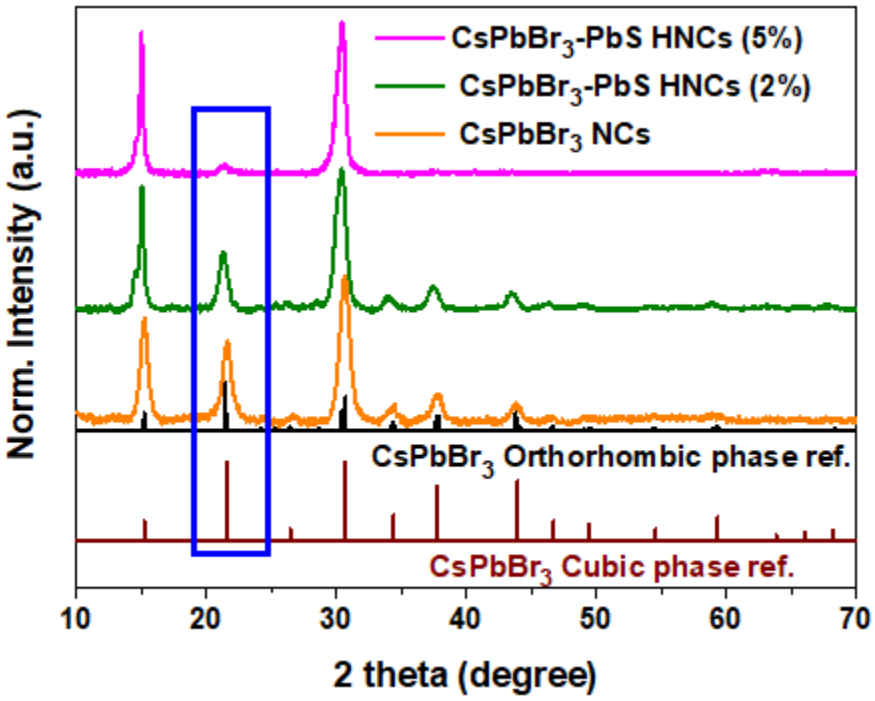

Fig. S3 a) Powder x-ray diffraction pattern (XRD) patterns of $CsPbBr_3$-PbS HNCs with 2% and 5% along with reference orthorhombic and cubic patterns. The intensity of the peak at 21.5^o is gradually decreased from 2% to 5% suggesting the growth of $CsPbBr_3$ perovskite along with peaks at ~15.2^o and 30.7^o according to HRTEM analysis. We note that with the broadening of XRD peaks for smaller size $CsPbBr_3$-PbS HNCs it is difficult to distinguish between orthorhombic and cubic phases both exhibiting similar Bragg`s angles for intense peaks.

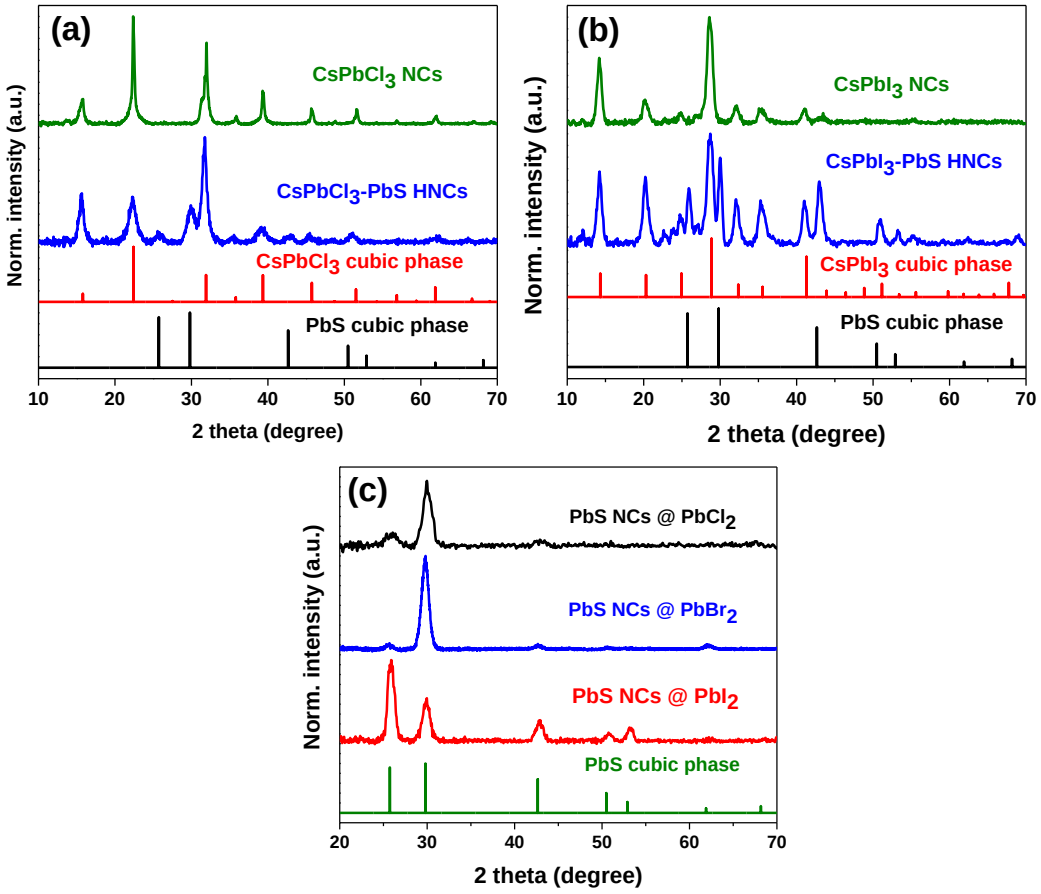

Fig. S4 a) XRD plot of $CsPbCl_3$ NCs and $CsPbCl_3$-PbS HNCs, b) XRD plot of $CsPbI_3$ NCs and $CsPbI_3$-PbS HNCs, and c) XRD plot of PbS NCs formed from upon thioacetamide and various lead sources i.e. lead chloride, lead bromide, and lead iodide, respectively.

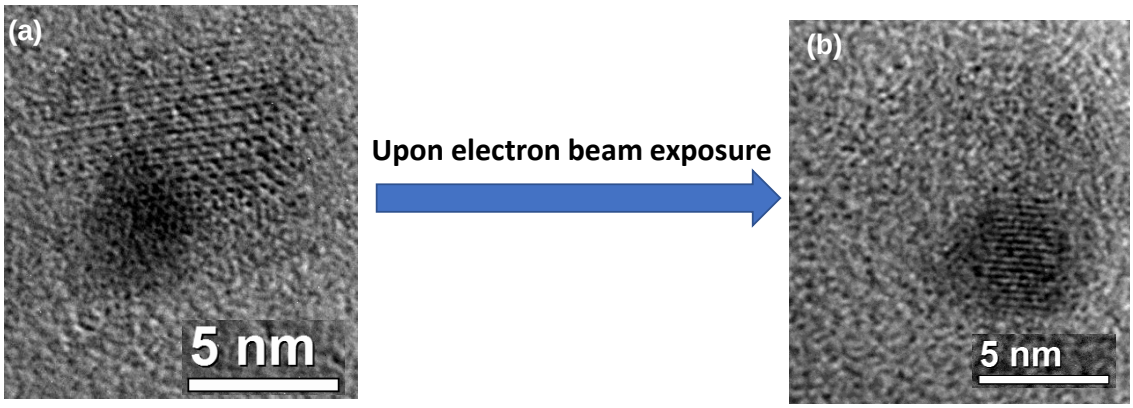

Fig. S5 a) and b) are TEM images of $CsPbBr_3$-PbS HNCs. Upon electron beam exposure under high-resolution imaging conditions, from a) to b) the damage of $CsPbBr_3$ perovskite which is attached to PbS particle can be observed. On the other hand, damage of perovskite is very less under low resolution.

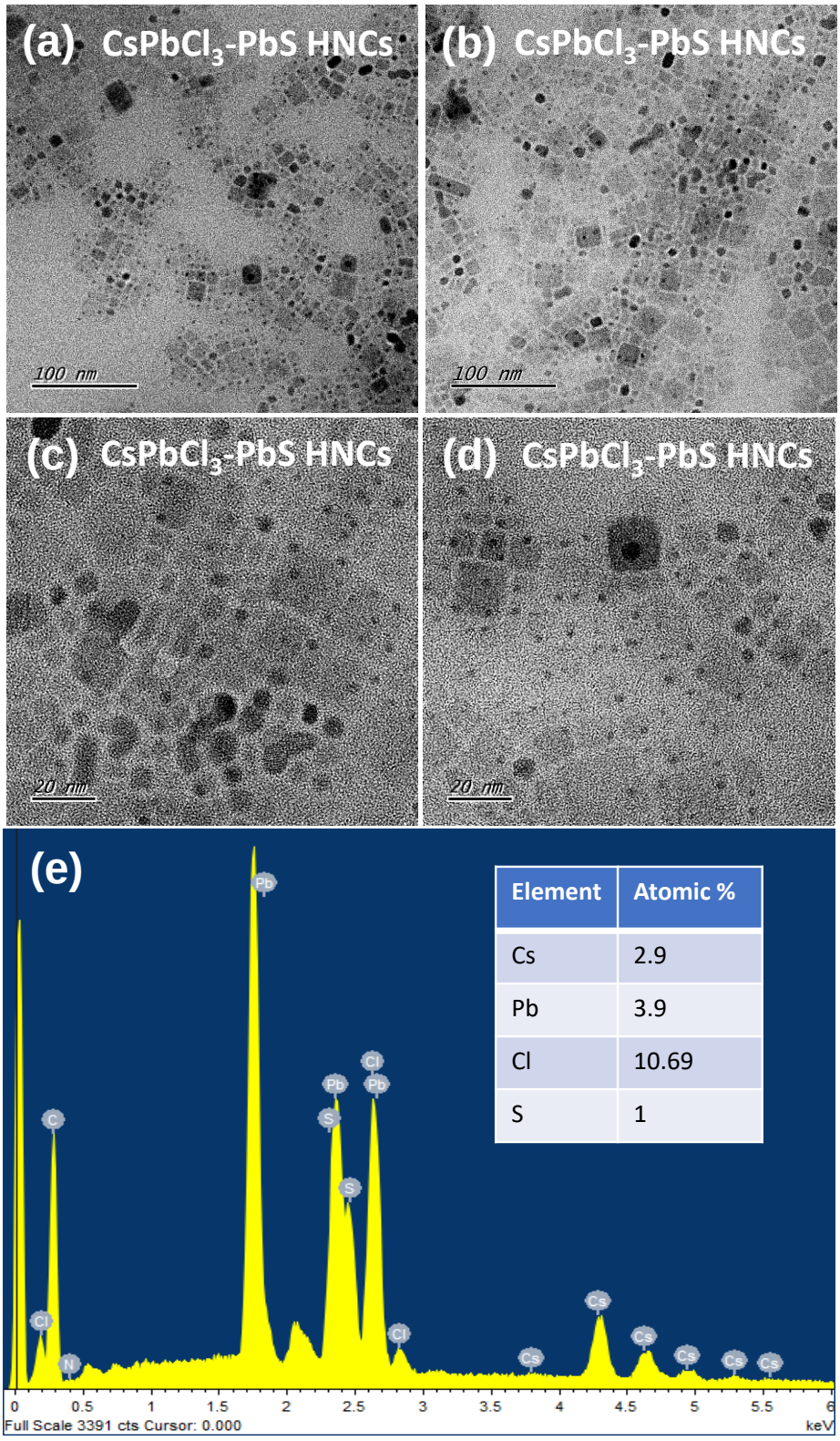

Fig. S6 a,b,c,d) TEM images of $CsPbCl_3$-PbS HNCs with different magnification at different locations where the more contrast (black) dot is PbS and lighter contrast part is $CsPbCl_3$. e) energy dispersive spectroscopy (**EDS**) analysis showing the elements present in the $CsPbCl_3$-PbS HNCs. Inset shows the elemental composition, for clarity elements like C, N, Si, and Pt were removed. Morphology of the $CsPbCl_3$-PbS HNCs is cubic similar to $CsPbBr_3$-PbS HNCs. Small inhomogeneity also there in $CsPbCl_3$-PbS HNCs.

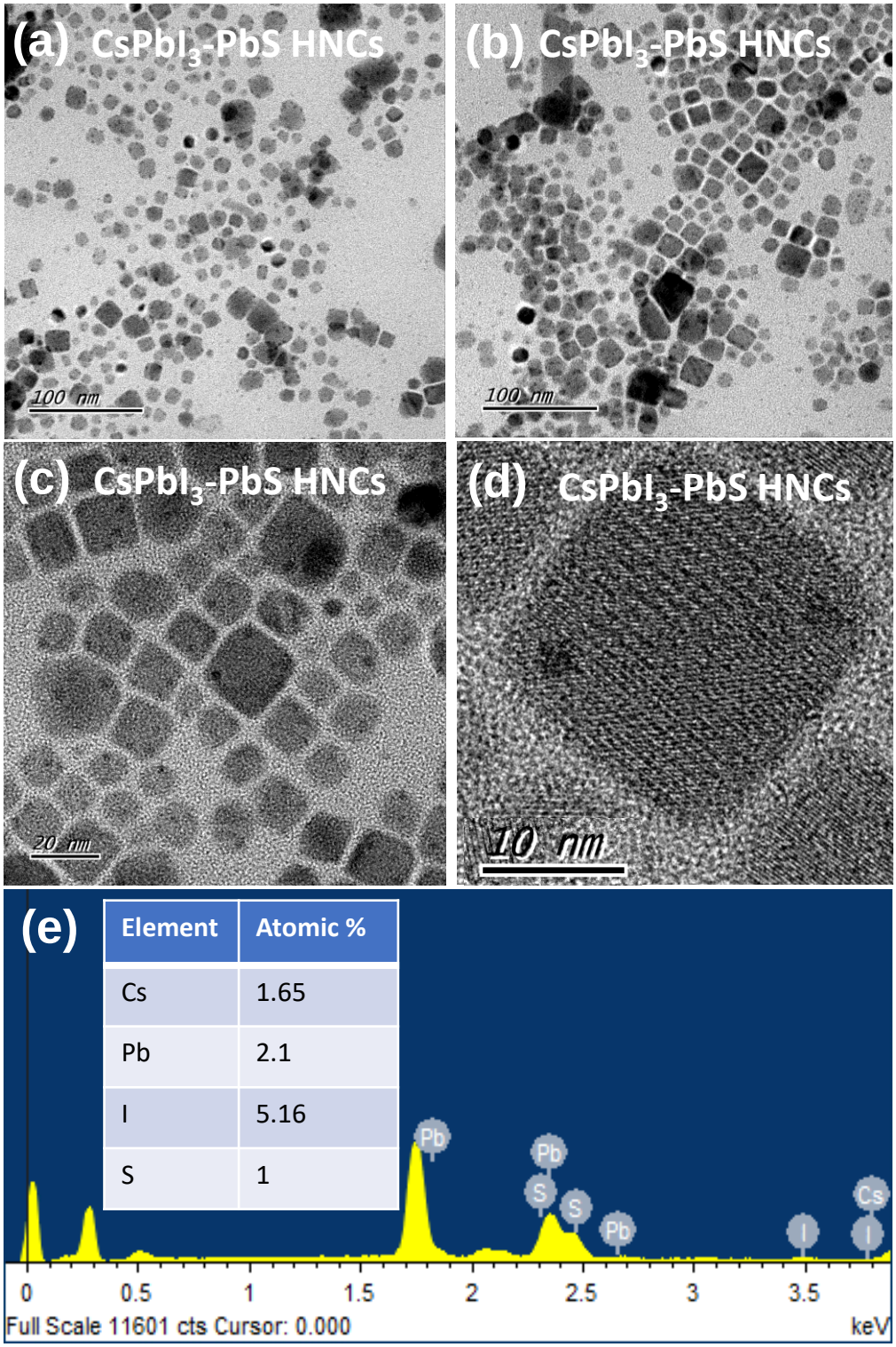

Fig. S7 TEM images of $CsPbI_3$-PbS HNCs with different magnification at different locations where the more contrast (black) dot is PbS and lighter contrast part is $CsPbI_3$. e) **EDS** analysis showing the elements present in the $CsPbI_3$-PbS HNCs. Inset shows the elemental composition, for clarity elements like C, N, Si, and Pt were removed. Morphology of the $CsPbI_3$-PbS HNCs is mostly cubic similar to $CsPbBr_3$-PbS HNCs.

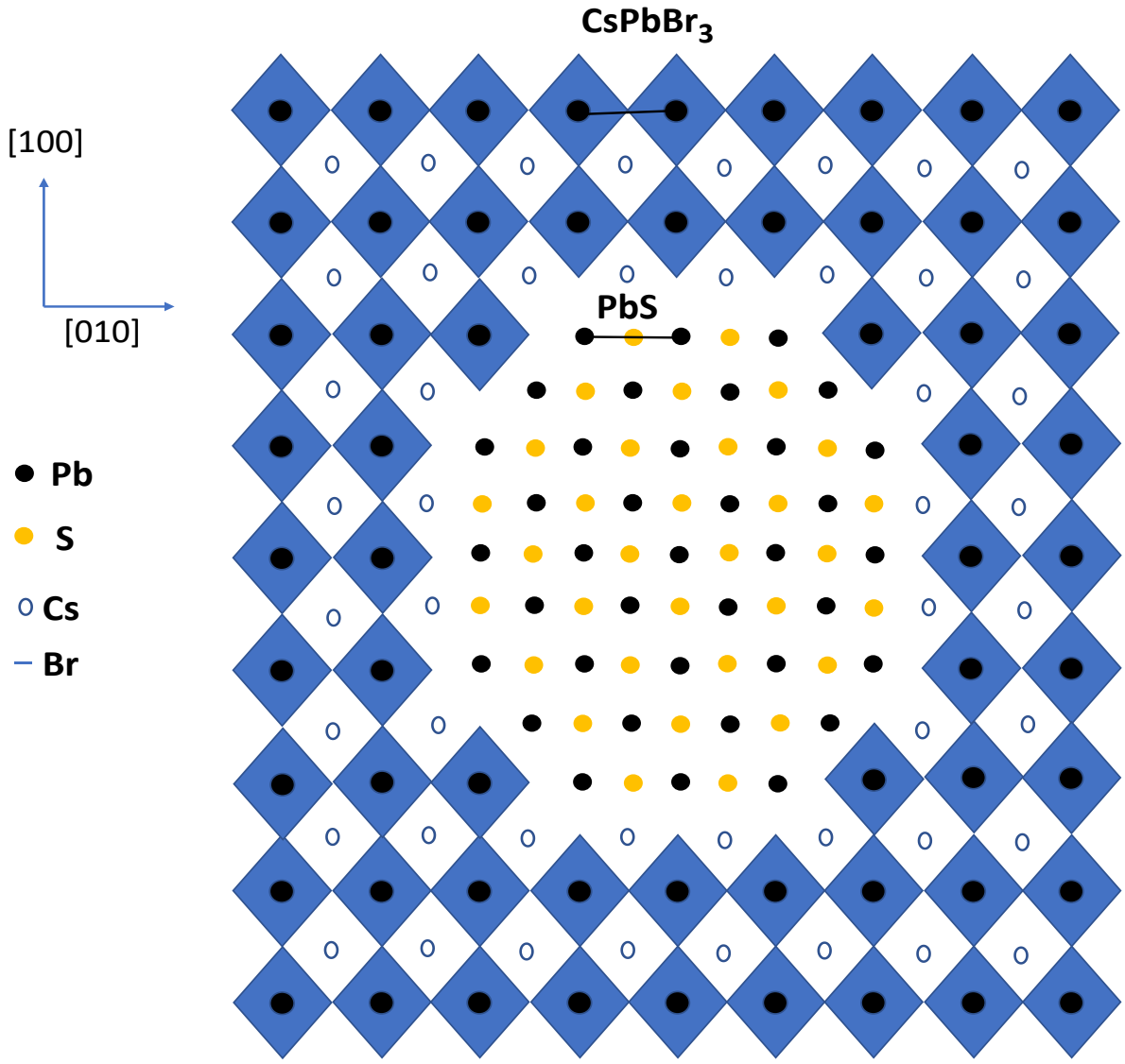

Fig. S8 Schematic representation of a $CsPbBr_3$ perovskite on PbS.[4]

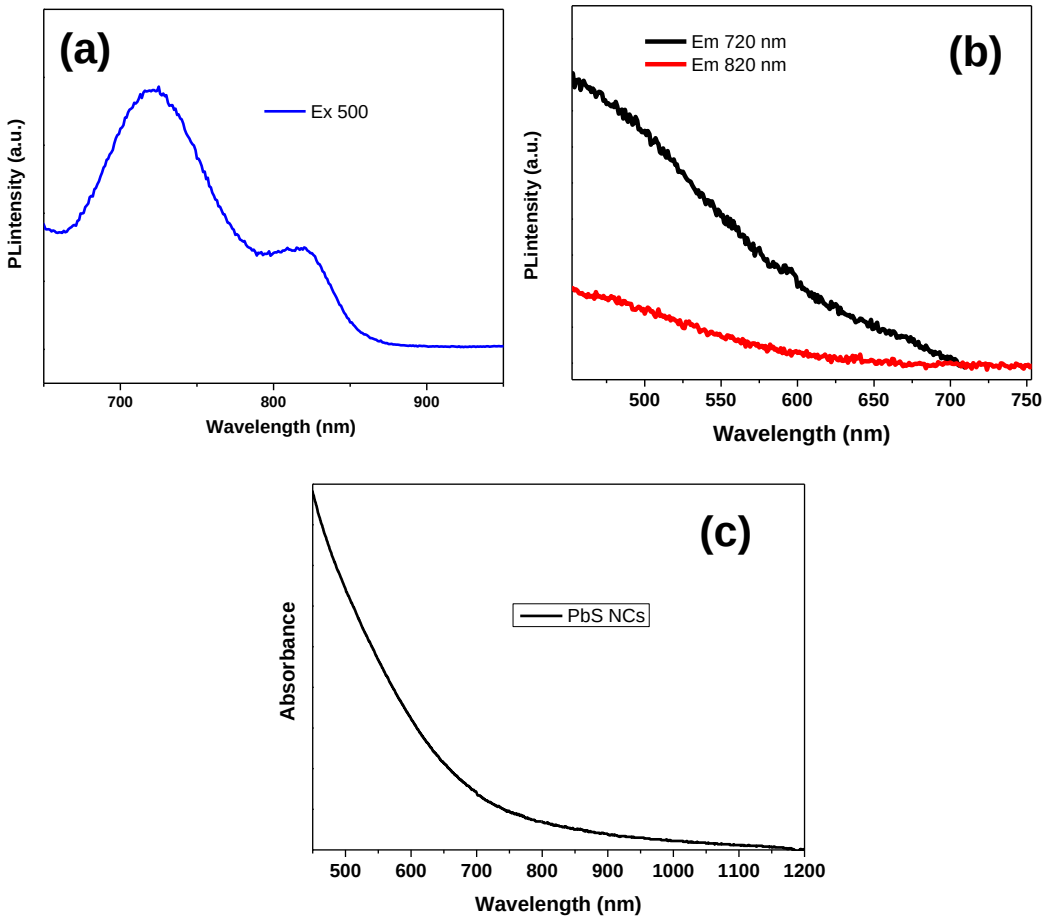

Fig. S9 a), b) and c) show emission, excitation, and absorption spectra of PbS NCs@$PbBr_2$.

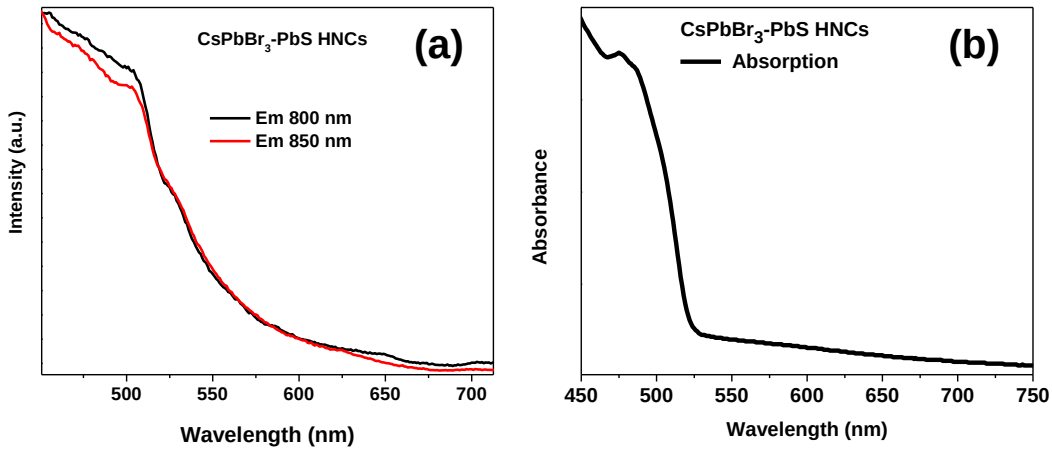

Fig S10. a), b) showing excitation spectra, and absorption spectra of $CsPbBr_3$-PbS HNCs, respectively.

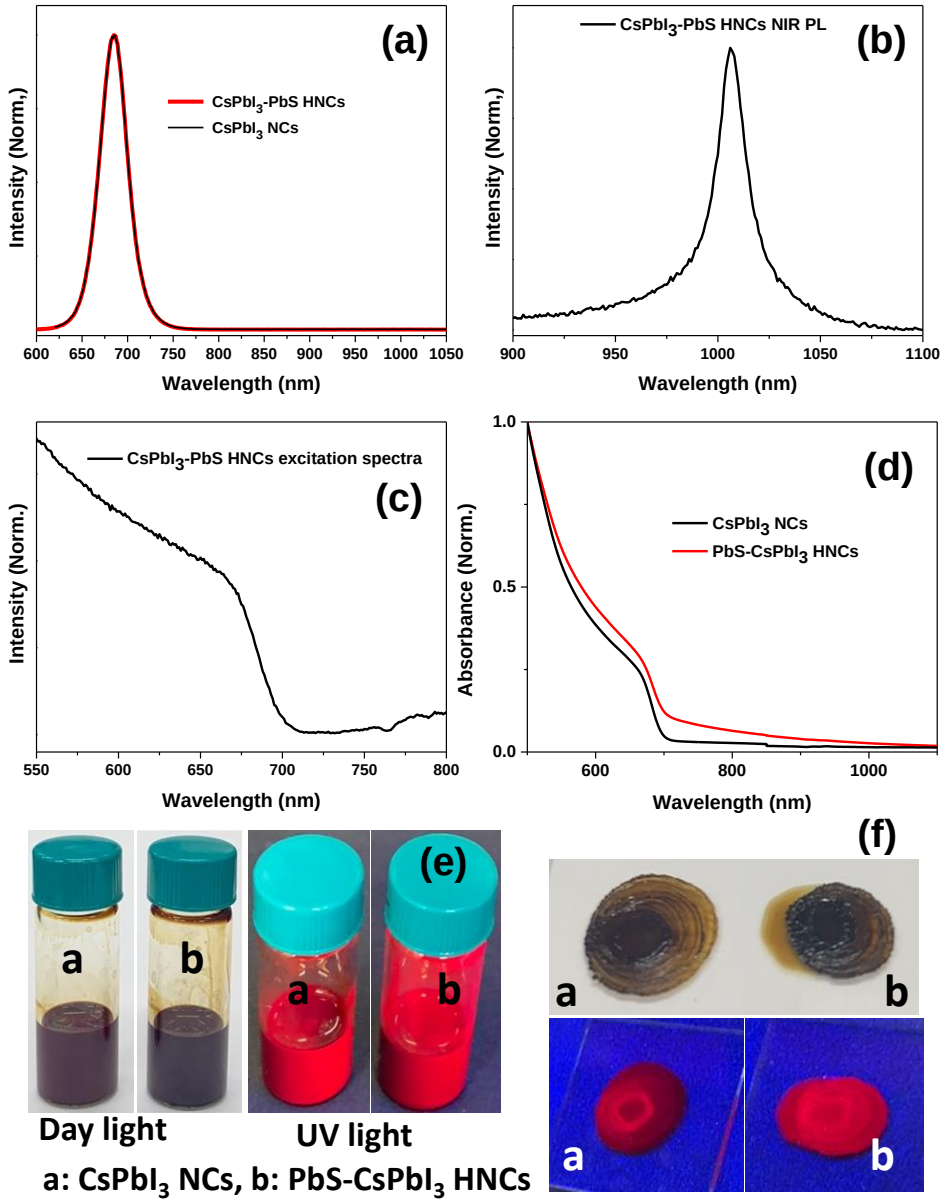

Fig. S11 a) PL spectra of $CsPbI_3$ NCs and $CsPbI_3$-PbS HNCs. b) PL spectrum of $CsPbI_3$-PbS HNCs in the NIR region. c) excitation spectrum of $CsPbI_3$-PbS HNCs at ~ 1000 nm. d) absorption spectra of $CsPbI_3$ NCs and $CsPbI_3$-PbS HNCs. NIR PL was also observed for $CsPbI_3$-PbS HNCs at ~ 1000 nm. The excitation spectrum of $CsPbI_3$-PbS HNCs also agrees with the absorption spectrum of $CsPbI_3$-PbS HNCs. However, further investigation is needed to confirm the energy/charge transfer in these HNCs. e,f) Photographs of the solutions and films of $CsPbI_3$ NCs and $CsPbI_3$-PbS HNCs under Day-light and 365 nm light irradiation. PLQYs of the solutions of $CsPbI_3$ NCs and $CsPbI_3$-PbS HNCs are found to be 45±5 and 60±4.

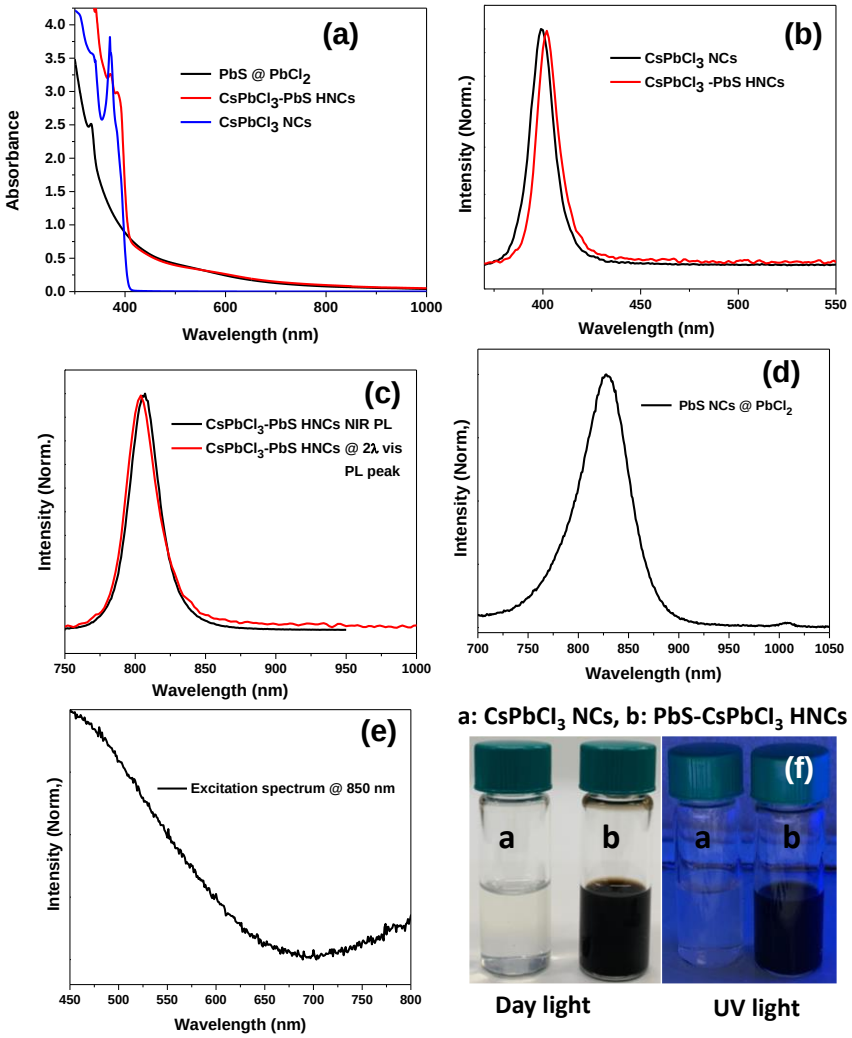

Fig. S12 a) absorption spectra of $CsPCl_3$ NCs, PbS NCs and $CsPbCl_3$-PbS HNCs. b and c) photoluminescence (PL) spectrum of $CsPbCl_3$ and $CsPbCl_3$-PbS HNCs in the visible region, NIR region respectively. d) PL spectrum and e) excitation spectrum of PbS NCs (prepared from $PbCl_2$). We note that it is difficult to distinguish the NIR PL of $CsPbCl_3$-PbS HNCs due to the overlap of 2λ peak i.e. 2xPL peak in the visible region of $CsPbCl_3$-PbS HNCs. Since we are not sure of NIR PL, therefore we did not study the electronic band alignment studies using UPS. f) Photographs of the solutions of $CsPbCl_3$ NCs and $CsPbCl_3$-PbS HNCs under Day-light and 365 nm light irradiation. The PLQYs of the solutions of $CsPbCl_3$ NCs and $CsPbCl_3$-PbS HNCs are found to be 3±1 and 5±2.

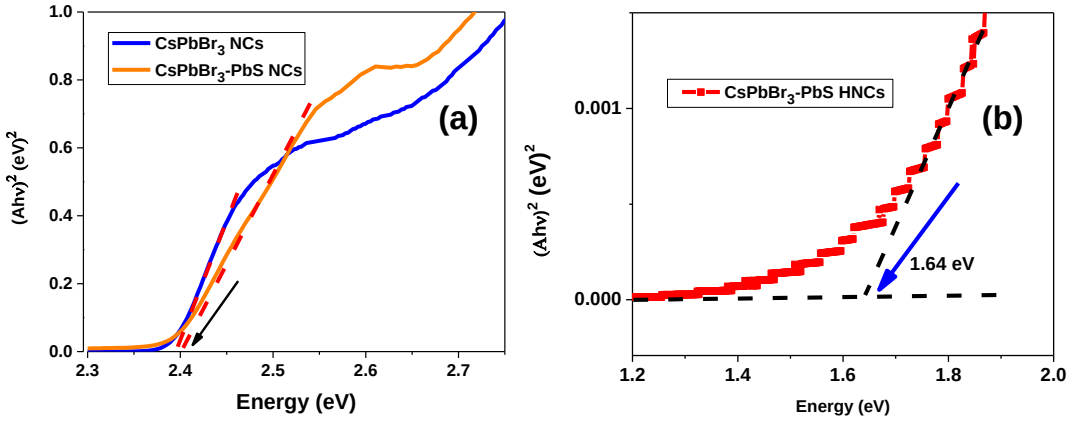

Fig. S13 $(Ahν)^2$ vs energy plot for a) $CsPbBr_3$-PbS HNCs and $CsPbBr_3$ NCs in the visible region, b) $CsPbBr_3$-PbS HNCs in the near infra-red region.

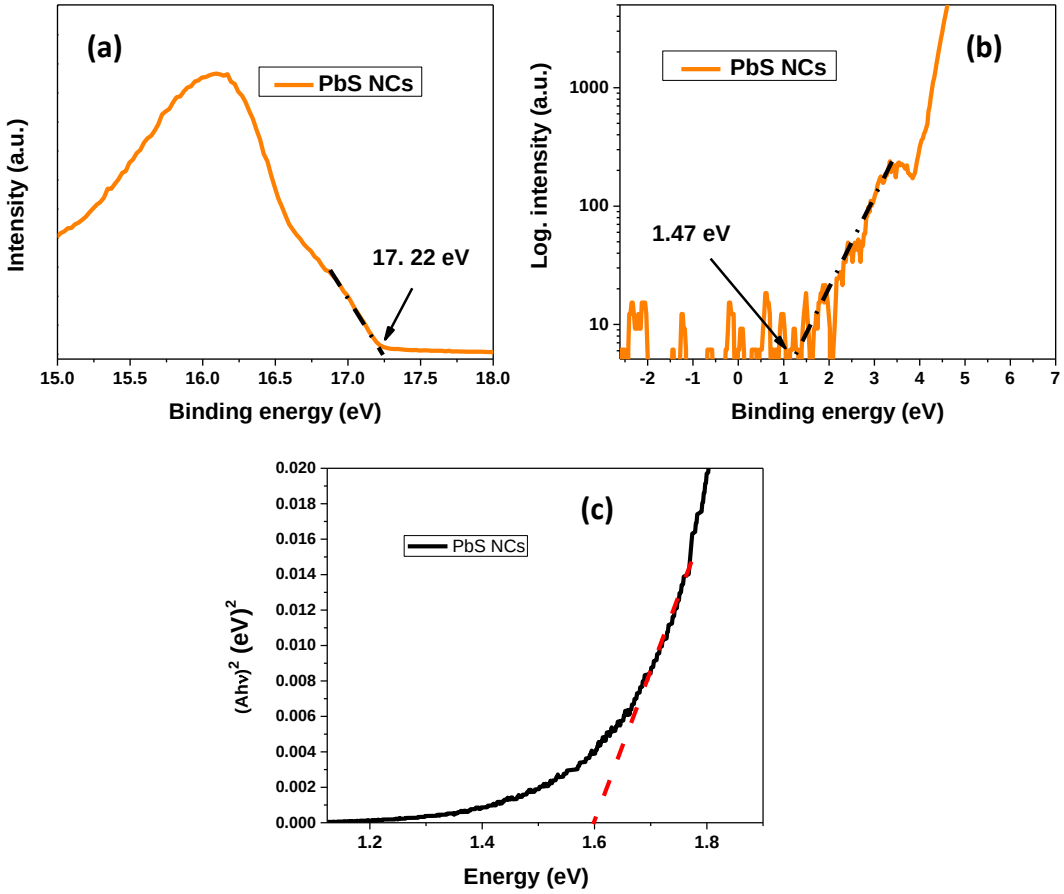

Fig. S14 a), b) Ultraviolet photoelectron spectroscopy (UPS) carried out for PbS NCs ((prepared from $PbBr_2$ as lead source and thioacetamide being a sulfur source) in the cut-off region and valance region, respectively. c) $(Ahν)^2$ vs energy plot for PbS NCs in the NIR region. .

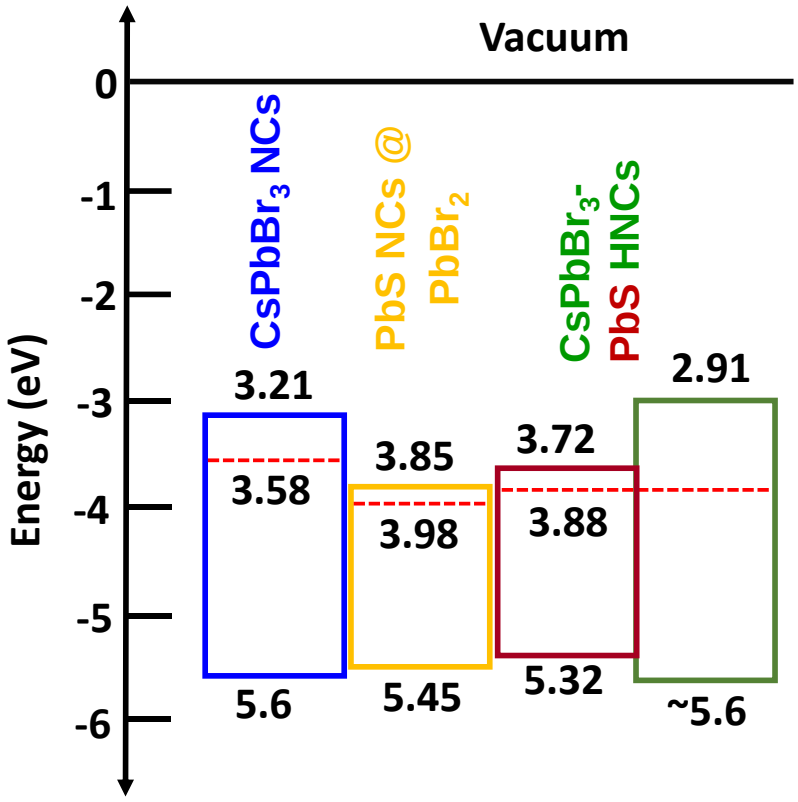

Fig. S15. Valance band maximum (VBM), conduction band minimum (CBM), and Fermi energy levels have been extracted from UPS and absorption spectra for $CsPbBr_3$ NCs, PbS NCs, and $CsPbBr_3$-PbS HNCs, respectively. The small changes in the VBM and CBM level of PbS and $CsPbBr_3$ for HNCs compared with the as-prepared samples can be attributed to the different chemical environments and size inhomogeneity. Further, it is evident from the Fourier Transform Infrared Spectroscopy (FTIR) analysis.

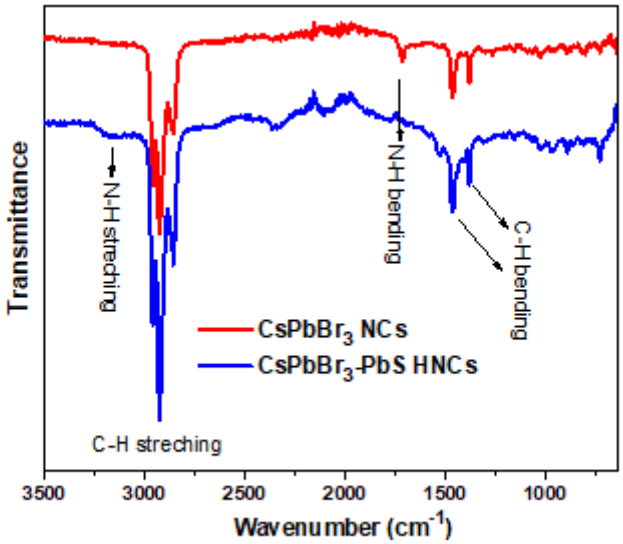

Fig. S16 FTIR spectrum of $CsPbBr_3$ NCs and $CsPbBr_3$-PbS HNCs. FTIR spectrum does not show any detectable contribution from C=S bond (thioacetamide) on the surface for $CsPbBr_3$-PbS HNCs.

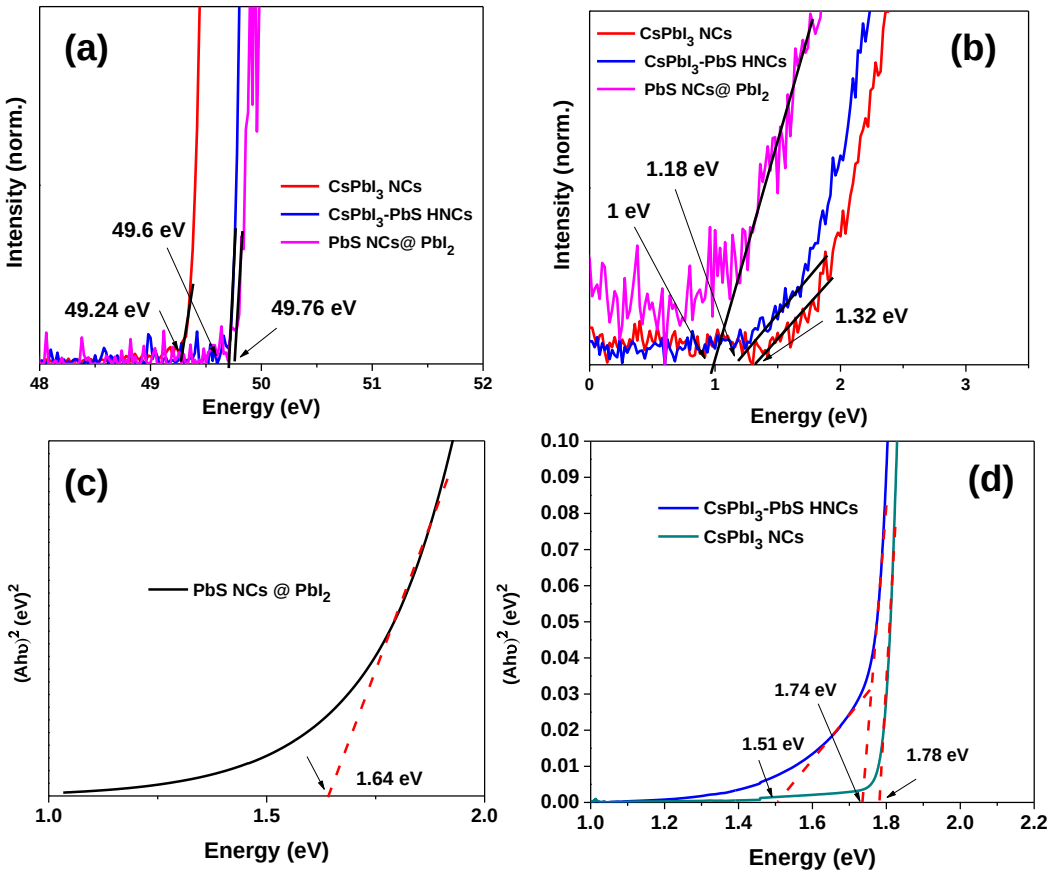

Fig. S17 a, b) UPS carried out for PbS NCs (prepared from PbI_2 as lead source and thioacetamide being a sulfur source) in the cut-off region and valance region, respectively. c,d) $(Ahν)^2$ vs energy plot for PbS NCs, $CsPbI_3$ NCs, and $CsPbI_3$-PbS HNCs respectively, in the NIR region.

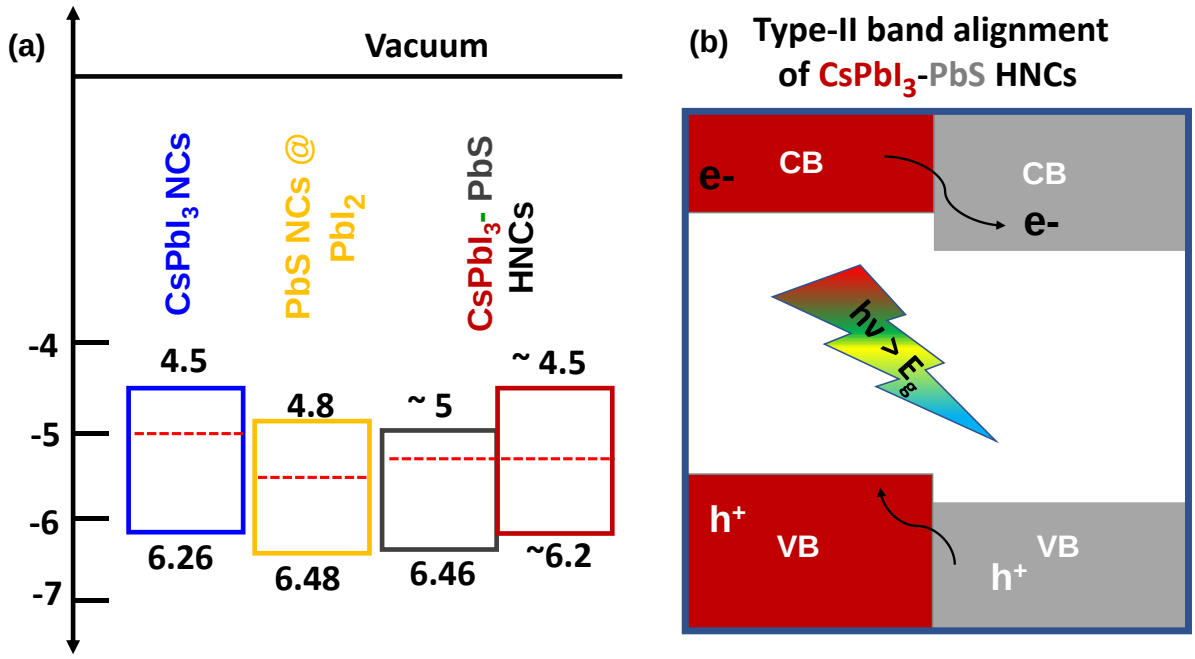

Fig. S18 Valance band maximum (VBM), conduction band minimum (CBM), and Fermi levels have been extracted from UPS and absorption spectra for $CsPI_3$ NCs, PbS NCs, and $CsPbI_3$-PbS HNCs, respectively. Schematic representation of type-II band alignment of $CsPbI_3$-PbS HNCs obtained from UPS and absorption spectroscopy. Type-II band alignment allows electron-hole charge separation across the interface upon illumination of light.

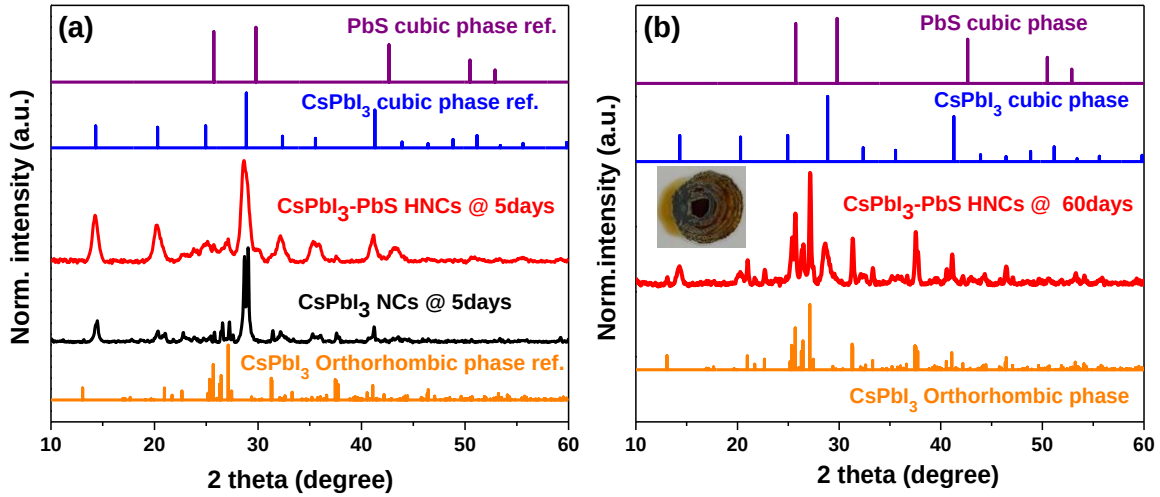

Fig. S19 a) and b) XRD patterns of the films of $CsPbI_3$ NCs and $CsPbI_3$-PbS HNCs on 5th and 60th day after making. Reference patterns of $CsPbI_3$ and PbS are also provided. In the period of 60 days film of $CsPbI_3$-PbS HNCs showing the co-existence of cubic and orthorhombic xrd peaks. Inset in Fig. b) shows the film $CsPbI_3$-PbS HNCs still looks brownish and it will take more days to complete conversion from cubic to orthorhombic phase.

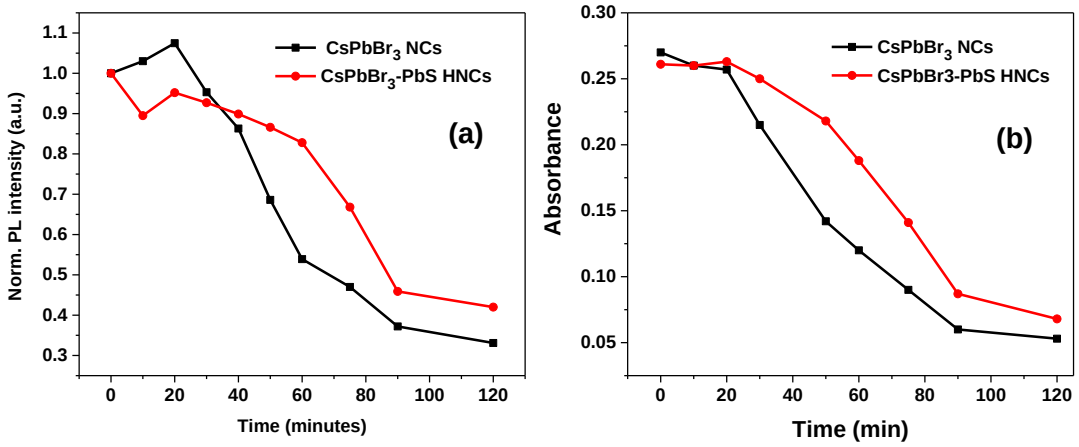

Fig. S20 We wanted to show the effect of polar solvents on these NCs because often NCs experience such polar environments in making optoelectronic devices and photocatalytic reactions. i.e., Coating of NCs on top of PEDOT, ZnO, TiO_2, SnO_2, etc layers which are often dispersed in polar solvents. Therefore, we did a simple experiment by adding a small amount of ethanol to the dispersions of NCs, and their UV and PL were checked over time to check the stability of our HNCs. To check the stability, 50 µL of ethanol was added to 3 mL NCs dispersion with similar concentration. a) shows the change in PL intensity, b) shows the change in the absorbance for $CsPbBr_3$ NCs and $CsPbBr_3$-PbS HNCs over a period of 120 minutes.

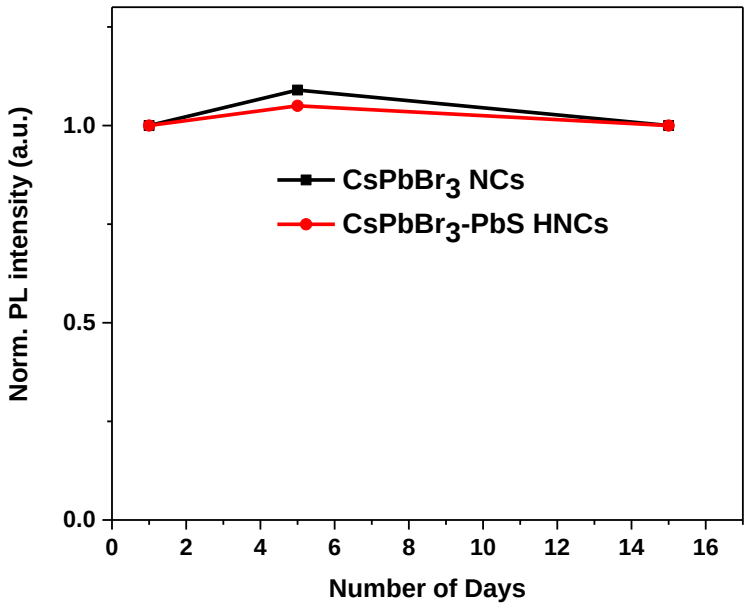

Fig. S21 Change in PL intensity of films of $CsPbBr_3$ NCs and $CsPbBr_3$-PbS HNCs under ambient conditions. The PL QY of $CsPbBr_3$ NCs is less than that of HNCs. This indicates that $CsPbBr_3$ NCs contain more defects than HNCs. It has been shown in the literature that oxygen passivates defects of perovskite films in the ambient air. This defect passivation has been

studied in solar cell applications.[5, 6] Probably, in our case also, $CsPbBr_3$ NCs containing more defects might be passivated by oxygen. However, further investigation is needed to verify this.

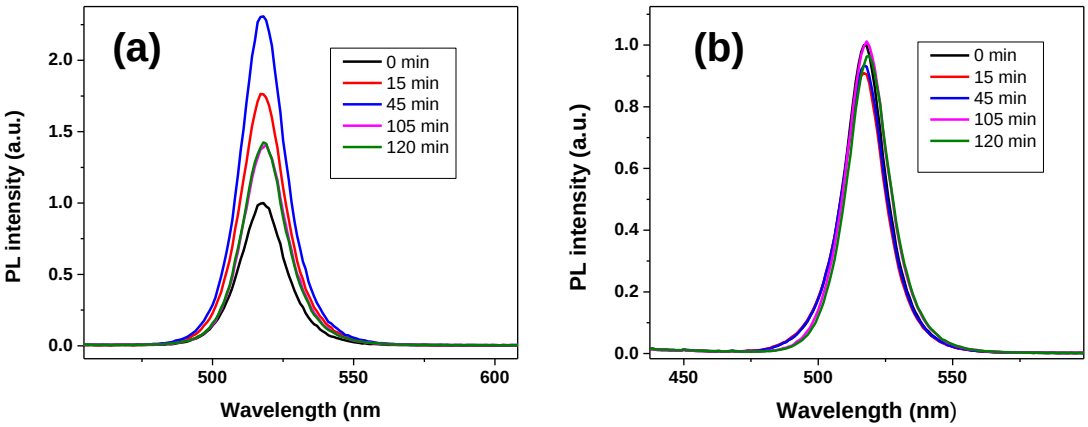

Fig. S22 Change in PL intensity of films of $CsPbBr_3$ NCs and $CsPbBr_3$-PbS HNCs under continuous 365 nm UV light source for 2 hours.

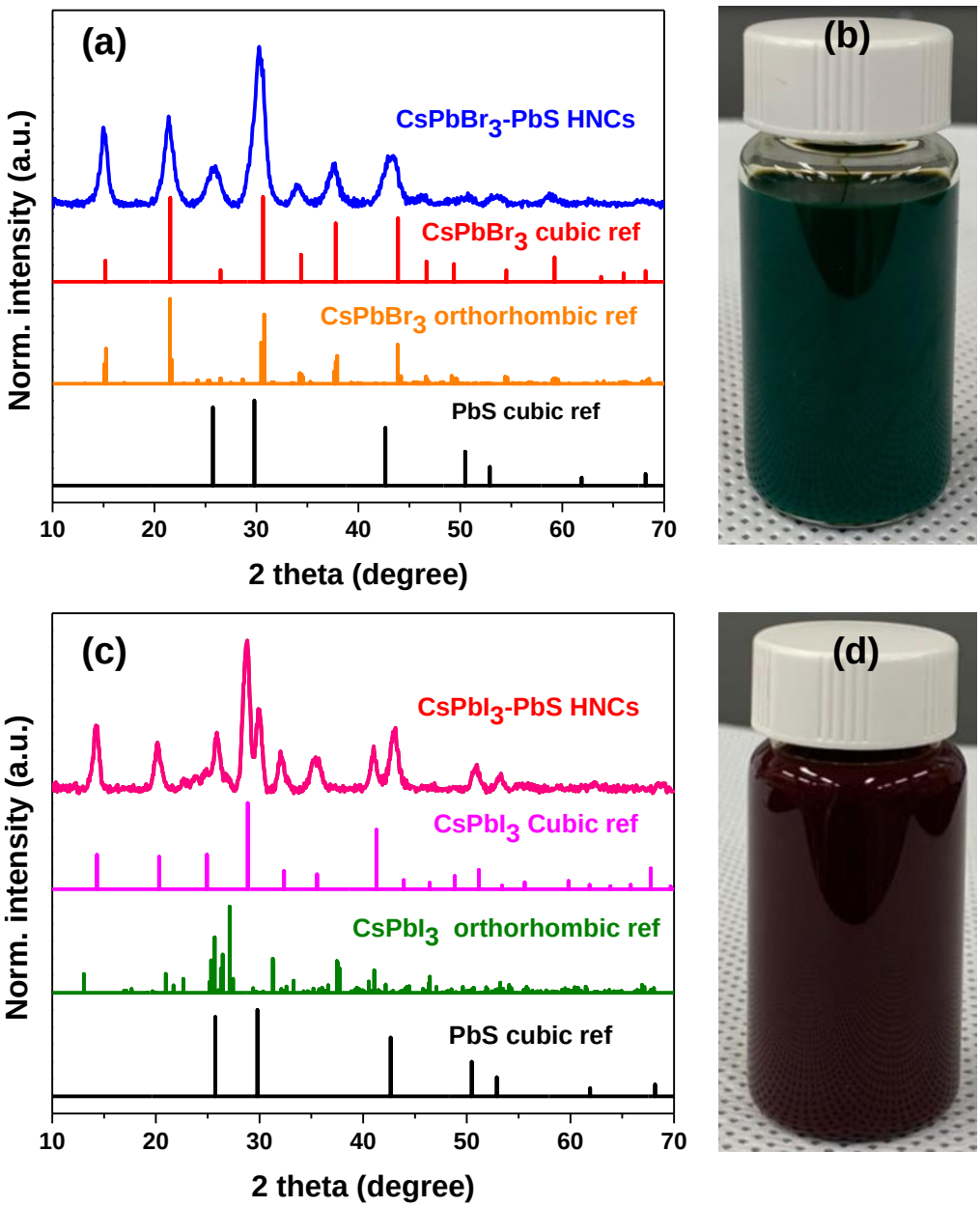

Fig. S23. a, c) XRD patterns and b, d) photograph of the large-scale synthesis of $CsPbBr_3$-PbS HNCs and $CsPbI_3$-PbS HNCs, respectively.

Table S1: The ^{207}Pb NMR parameters of the nanocrystal samples determined via Gaussian/Lorentzian fitting (except for $CsPbBr_3$ which was simulated with a *J*-coupling multiplet with $^1J(^{207}Pb\text{-}^{79/81}Br)$ = 2.3 ± 0.3 KHz and individual spikelet FWHM = 2.64 ± 0.3 kHz).

Nanocrystals	**Assignment**	**δ_{iso}(^{207}Pb)** (ppm)	**FWHM** (KHz)	**Relative intensity** (%)
$CsPbBr_3$	-	260 ± 1	-	-
PbS	-	1380 ± 30	63 ± 8	-
$CsPbBr_3$-PbS	$CsPbBr_3$	240 ± 10	22 ± 3	74.2
	PbS	1270 ± 50	110 ± 10	25.8

Table S2: The ^{133}Cs NMR parameters of the nanocrystal samples determined via Gaussian/Lorentzian fitting

Nanocrystals	**Assignment**	**δ_{iso}(^{133}Cs)** (ppm)	**FWHM** (kHz)	**Relative intensity** (%)
$CsPbBr_3$	Bulk	120.0 ± 0.2	0.29 ± 0.04	36.6
	Near-surface layers	116.7 ± 0.6	0.73 ± 0.09	24.9
		105 ± 2	2.1 ± 0.3	38.5
$CsPbBr_3$-PbS	$CsPbBr_3$	116 ± 1	0.75 ± 0.09	3.3
	Distorted $CsPbBr_3$	101 ± 2	2.1 ± 0.2	88.8
	Boundary sites	193 ± 2	2.4 ± 0.3	5.3
		170.1 ± 1	1.6 ± 0.2	2.6

REFERENCES

(1). Hu, L.; Zhao, Q.; Huang, S.; Zheng, J.; Guan, X.; Patterson, R.; Kim, J.; Shi, L.; Lin, C.-H.; Lei, Q.; Chu, D.; Tao, W.; Cheong, S.; Tilley, R. D.; Ho-Baillie, A. W. Y.; Luther, J. M.; Yuan, J.; Wu, T., Flexible and Efficient Perovskite Quantum Dot Solar Cells via Hybrid Interfacial Architecture. *Nat. Commun.* **2021,** *12*, 466.

(2). Massiot, D.; Fayon, F.; Capron, M.; King, I.; Le Calvé, S.; Alonso, B.; Durand, J.-O.; Bujoli, B.; Gan, Z.; Hoatson, G., Modelling One- and Two-Dimensional Solid-State NMR Spectra. *Magn. Reson. Chem.* **2002,** *40*, 70-76.

(3). La Mer V.K.; Dinegar R.H. Theory, Production and Mechanism of Formation of Monodispersed Hydrosols. *J. Am. Chem. Soc*. **1950**, *72*, 4847.

(4). Liu, M.; Chen, Y.; Tan, C.-S.; Quintero-Bermudez, R.; Proppe, A. H.; Munir, R.; Tan, H.; Voznyy, O.; Scheffel, B.; Walters, G.; Kam, A. P. T.; Sun, B.; Choi, M.-J.; Hoogland, S.; Amassian, A.; Kelley, S. O.; García de Arquer, F. P.; Sargent, E. H., Lattice Anchoring Stabilizes Solution-Processed Semiconductors. *Nature* **2019,** *570*, 96-101.

(5). Huang, L.; Ge, Z.; Zhang, X.; Zhu, Y., Oxygen-Induced Defect-Healing and Photo-Brightening of Halide Perovskite Semiconductors: Science and Application. *J. Mater. Chem. A* **2021,** *9*, 4379-4414.

(6). Liu, S.-C.; Li, Z.; Yang, Y.; Wang, X.; Chen, Y.-X.; Xue, D.-J.; Hu, J.-S., Investigation of Oxygen Passivation for High-Performance All-Inorganic Perovskite Solar Cells. *J. Am. Chem. Soc.* **2019,** *141*, 18075-18082.